Supporting Information

X-ray Absorption Spectroscopy Systematics at the Tungsten L-Edge

Upul Jayarathne,[†,#] *Perumalreddy Chandrasekaran,*[†,‖] *Angelique F. Greene,*[†] *Joel T. Mague,*[†] *Serena DeBeer,*[⊥,▽] *Kyle M. Lancaster,*[⊥] *Stephen Sproules,**[,§] *and James P. Donahue**[,†]

[†]Department of Chemistry, Tulane University, 6400 Freret Street, New Orleans, Louisiana 70118, United States, [‖]Department of Chemistry and Biochemistry, Lamar University, Beaumont, Texas 77710, United States, [⊥]Department of Chemistry and Chemical Biology, Baker Laboratory, Cornell University, Ithaca, New York 14853, United States, [▽]Max-Planck-Institut für Chemische Energiekonversion, Stiftstrasse 34-36, D-45470, Mülheim an der Ruhr, Germany, and [§]WestCHEM, School of Chemistry, University of Glasgow, Glasgow G12 8QQ, United Kingdom

[#]Present address: Department of Chemistry, University of Illinois at Chicago, 845 West Taylor Street, MC 111, Chicago, Illinois 60607, United States

E-mail: stephen.sproules@glasgow.ac.uk; donahue@tulane.edu

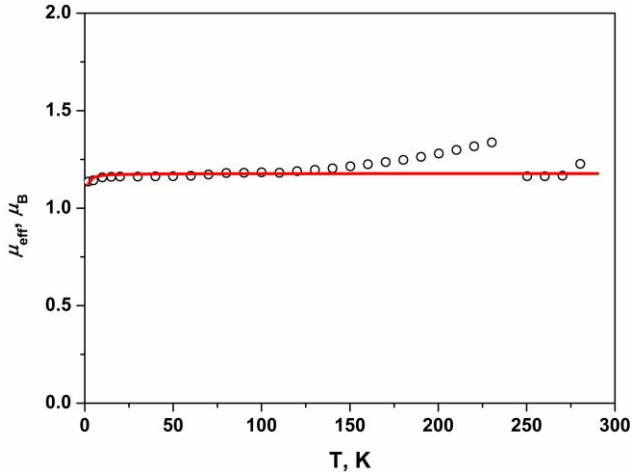

Figure S1. Temperature dependence of the magnetic moment, μ_{eff}, μ_B, of powdered sample of $[W^{III}Cl_2(dppe)_2][PF_6]$ measured in a 1 T external field. Experimental data are shown as filled circles, and the red line indicates a best fit: $S = {}^1/_2$; $g = 1.35$; TIP = -157×10^{-6} cm^3 mol^{-1}; $\theta_W = -0.09$ K.

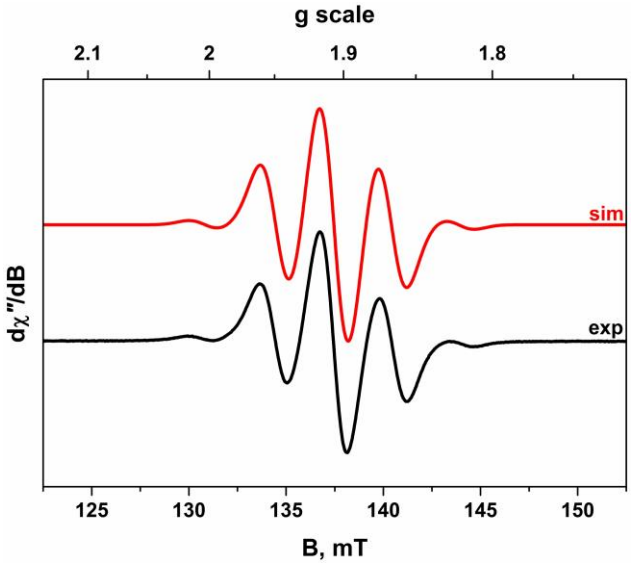

Figure S2. S-band EPR spectrum of $[W^{V}(NPh)Cl_3(PMe_3)_2]$ recorded in CH_2Cl_2/THF solution at 190 K (experimental conditions: frequency, 3.6684 GHz; power 2.0 mW; modulation, 0.5 mT). Experimental data are depicted by the black line and simulation in red: g_{iso} = 1.903; A_W = 60 × 10^{-4} cm^{-1}; A_P = 26 × 10^{-4} cm^{-1}.

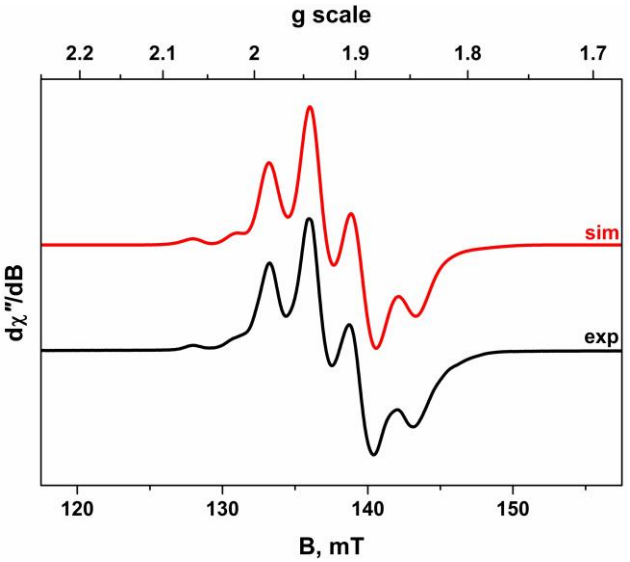

Figure S3. S-band EPR spectrum of $[W^{V}(NPh)Cl_3(PMe_3)_2]$ recorded in CH_2Cl_2/THF solution at 30 K (experimental conditions: frequency, 3.7005 GHz; power 0.2 mW; modulation, 0.2 mT). Experimental data are depicted by the black line and simulation in red: g = (1.9372, 1.9066, 1.8829); A_W = (91, 116, -25) × 10^{-4} cm^{-1}; A_P = (25, 28, 25) × 10^{-4} cm^{-1}.

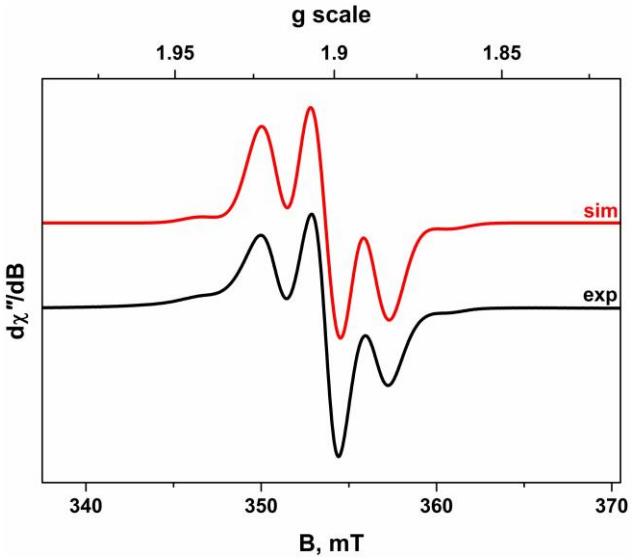

Figure S4. X-band EPR spectrum of $[W^{V}(NPh)Cl_3(PMe_3)_2]$ recorded in CH_2Cl_2/THF solution at 190 K (experimental conditions: frequency, 9.4182 GHz; power 0.2 mW; modulation, 0.2 mT). Experimental data are depicted by the black line and simulation in red: g_{iso} = 1.903; A_W = 60 × 10^{-4} cm^{-1}; A_P = 26 × 10^{-4} cm^{-1}.

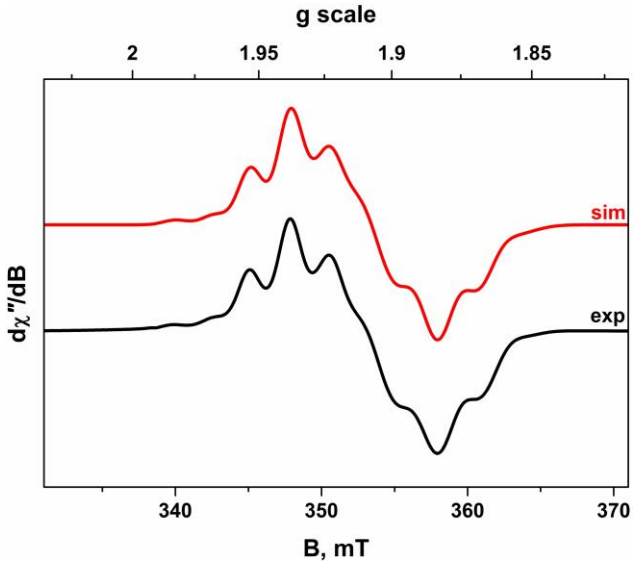

Figure S5. X-band EPR spectrum of $[W^{V}(NPh)Cl_3(PMe_3)_2]$ recorded in CH_2Cl_2/THF solution at 30 K (experimental conditions: frequency, 9.4352 GHz; power 0.006 mW; modulation, 0.5 mT). Experimental data are depicted by the black line and simulation in red: g = (1.9372, 1.9066, 1.8829); A_W = (91, 116, -25) × 10^{-4} cm^{-1}; A_P = (25, 28, 25) × 10^{-4} cm^{-1}.

Table S1. Experimental (L_3 and L_2-edge) and Calculated Ligand Field Splitting (eV) for Complexes

Compound	L_3	L_2	Calcd
$[W^{II}Cl_2(PMePh_2)_4]$	2.3	2.2	2.9
$[W^{III}Cl_2(dppe)_2][PF_6]$	3.6	3.3	3.7
$[W^{IV}Cl_4(PMePh_2)_2]$	3.0	2.7	3.3
$[W^{V}(NPh)Cl_3(PMe_3)_2]$	1.1	1.6	1.6
$[W^{VI}Cl_6]$	3.3	3.4	3.3

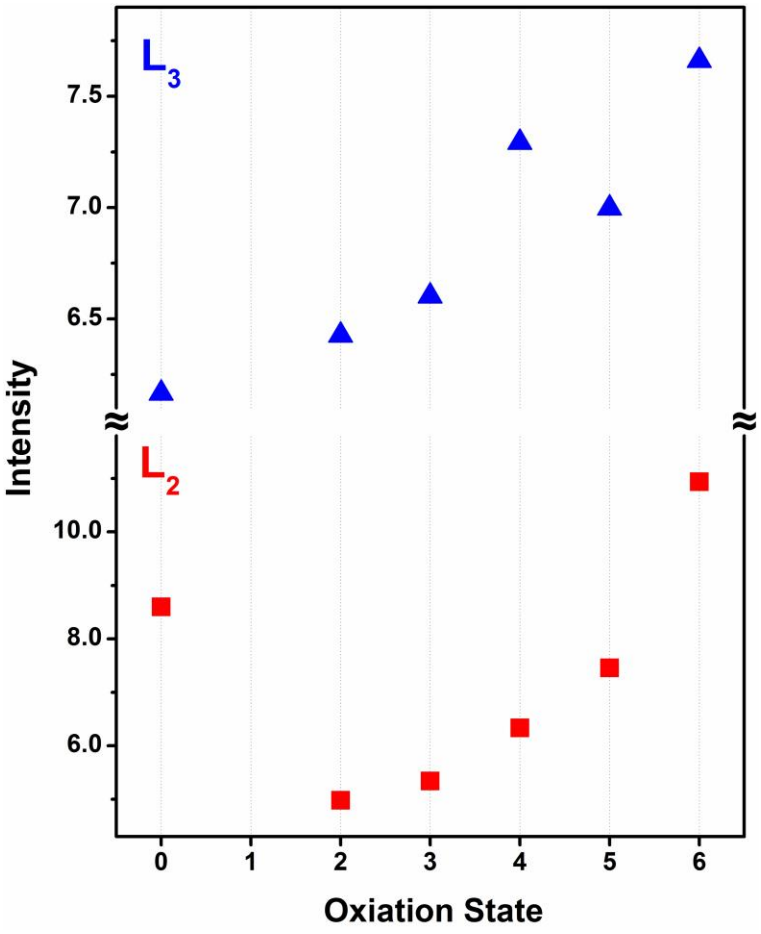

Figure S6. Comparison of the L_3- (▲) and L_2-edge (■) intensities of the six reference compounds $[W^0(PMe_3)_6]$, $[W^{II}Cl_2(PMePh_2)_4]$, $[W^{III}Cl_2(dppe)_2][PF_6]$, $[W^{IV}Cl_4(PMePh_2)_2]$, $[W^V(NPh)Cl_3(PMe_3)_2]$, and $[W^{VI}Cl_6]$.

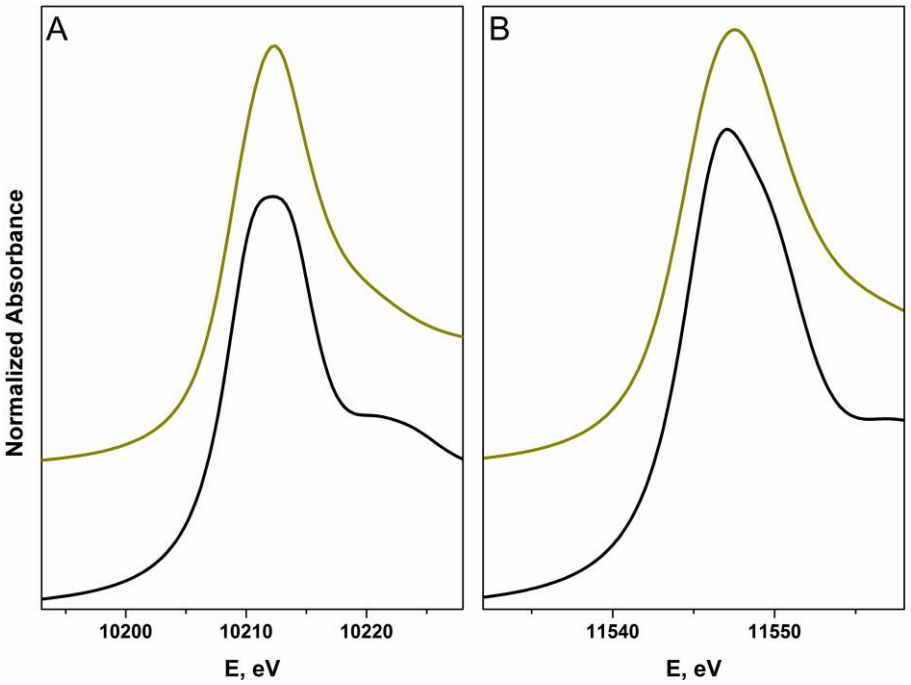

Figure S7. Comparison of the normalized W L_3- (panel A) and L_2-edge (panel B) X-ray absorption spectra of $[W^{VI}Cl_6]$ (black) and $[W^{VI}(xylidene)_3]$ (dark yellow).

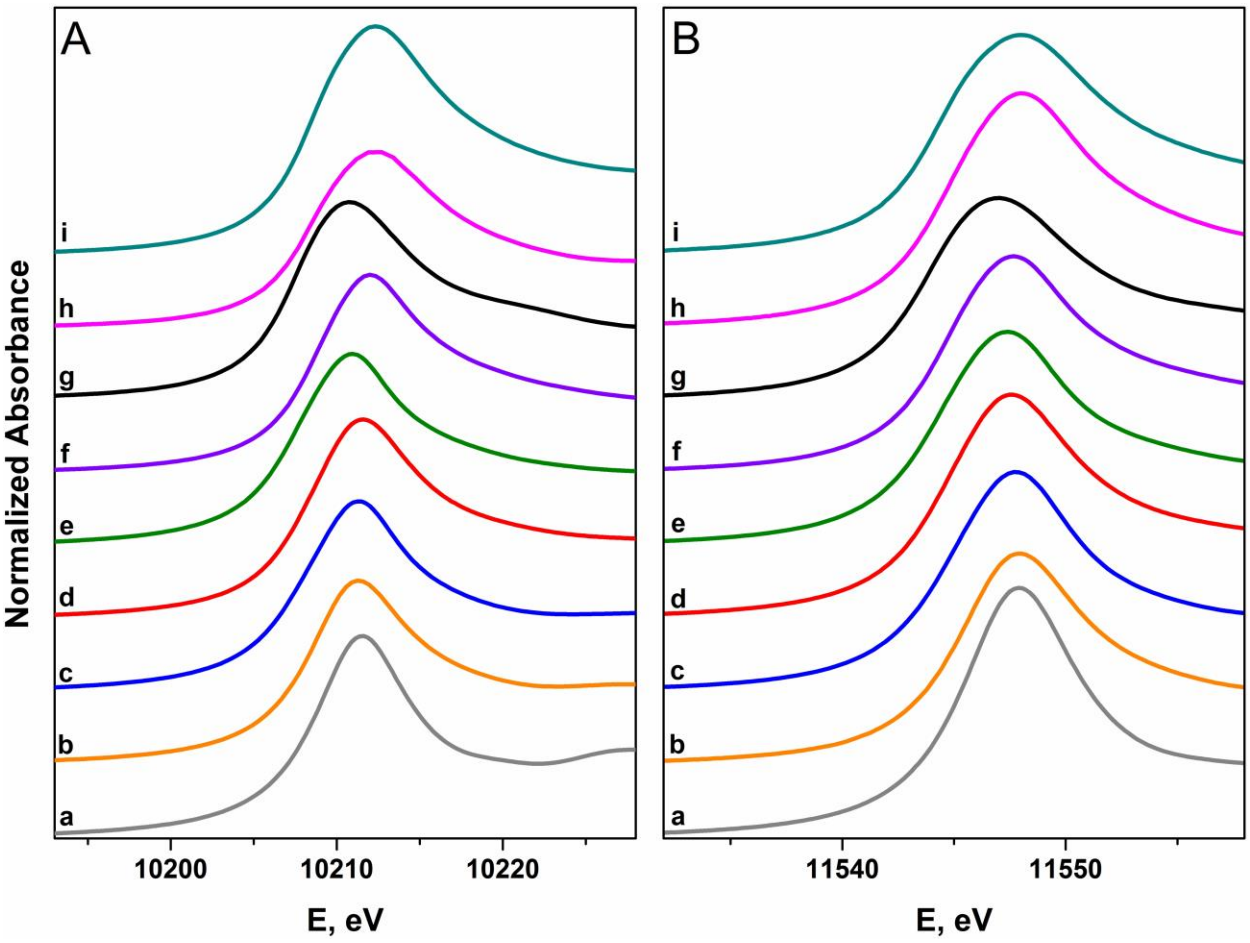

Figure S8. Comparison of the normalized W L_3- (panel A) and L_2-edge (panel B) X-ray absorption spectra of (a) $[W^0(CO)_6]$, (b) $[W^0(Me_2pipdt)(CO)_4]$, (c) $[W^{II}(mdt)(CO)_4]$, (d) $[W^{II}(mdt)(CO)_2(PMe_3)_2]$, (e) $[W^{IV}(mdt)_2(CO)_2]$, (f) $[W^{IV}(mdt)_2(CO)(PMe_3)]$, (g) $[W^{IV}(mdt)_2(PMe_3)_2]$, (h) $[W^{IV}(mdt)_2(CN^tBu)_2]$, (i) $[NEt_4]_2[W^{IV}(mdt)_2(CN)_2]$.

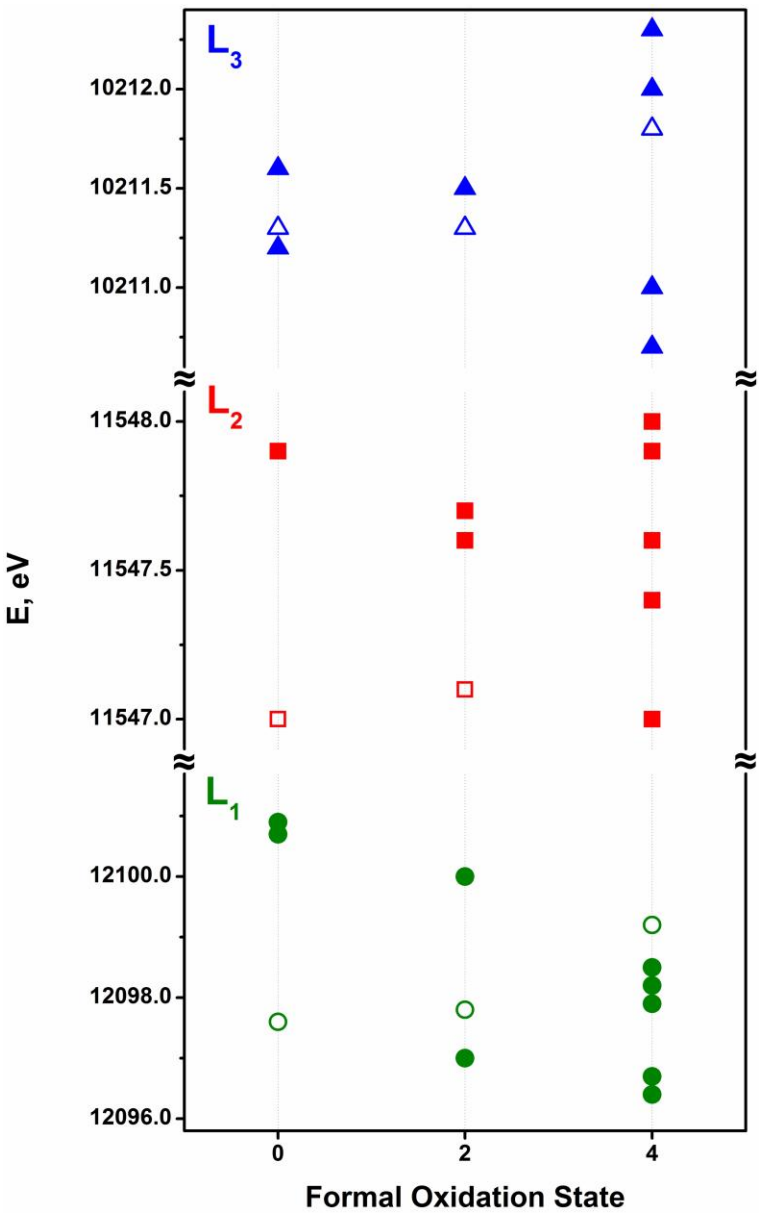

Figure S9. Comparison of the L_3- (▲), L_2- (■) and L_1-edge (●) energies of formally W^0 compounds $[W^0(CO)_6]$ and $[W^0(Me_2pipdt)(CO)_4]$, W^{II} complexes $[W^{II}(mdt)(CO)_4]$ and $[W^{II}(mdt)(CO)_2(PMe_3)_2]$, and W^{IV} compounds $[W^{IV}(mdt)_2(CO)_2]$, $[W^{IV}(mdt)_2(CO)(PMe_3)]$, $[W^{IV}(mdt)_2(PMe_3)_2]$, $[W^{IV}(mdt)_2(CN^tBu)_2]$, and $[NEt_4]_2[W^{IV}(mdt)_2(CN)_2]$, with their respective standards, $[W^0(PMe_3)_6]$, $[W^{II}Cl_2(PMePh_2)_4]$, and $[W^{IV}Cl_4(PMePh_2)_2]$, represented by the open shapes.

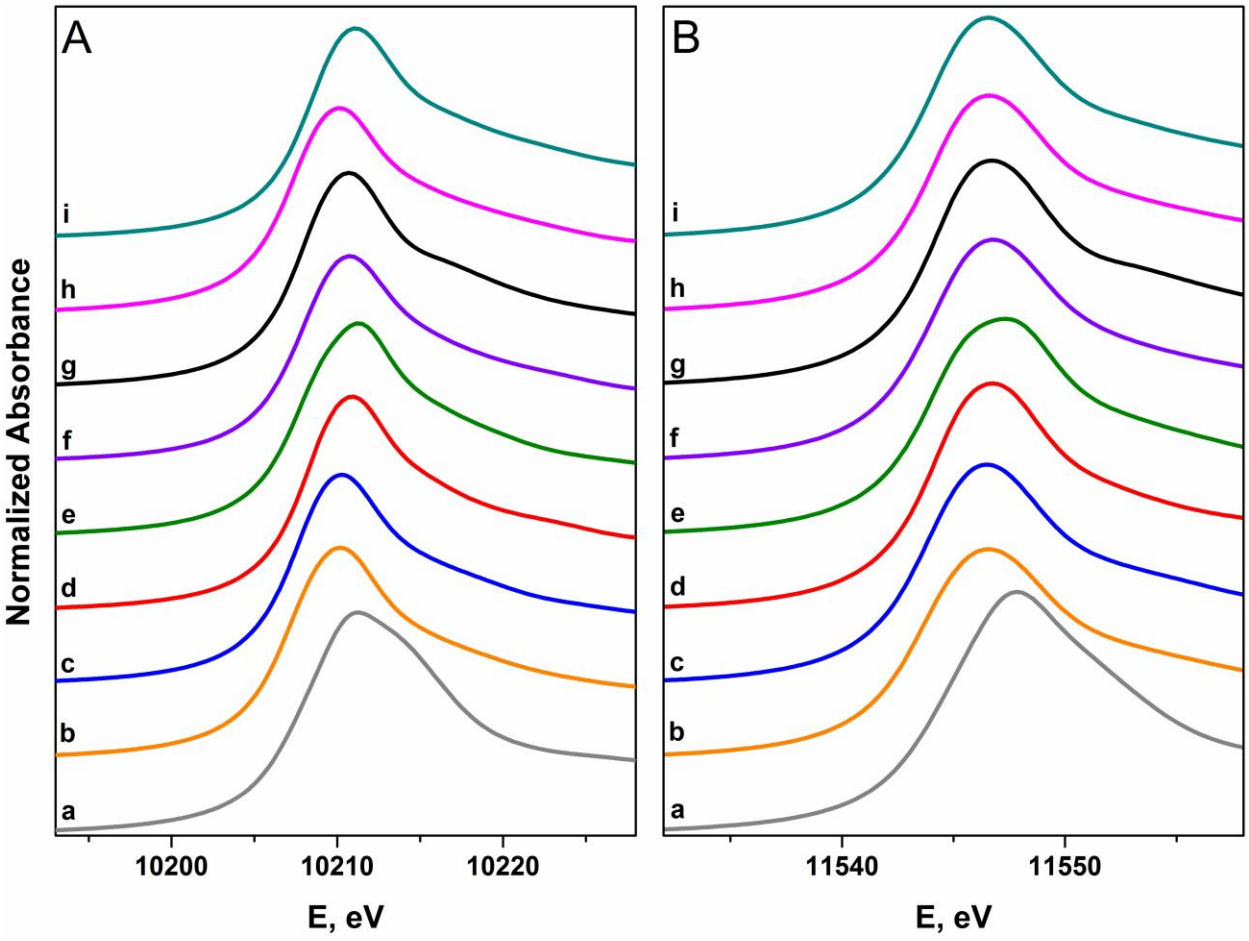

Figure S10. Comparison of the normalized W L_3- (panel A) and L_2-edge (panel B) X-ray absorption spectra of (a) $[PPh_4]_2[W^{IV}(mnt)_3]$, (b) $[PPh_4]_2[W^{IV}(bdt)_3]$, (c) $[NEt_4]_2[W^{IV}(bdt)_3]$, (d) $[NEt_4]_2[W^{IV}(mdt)_3]$, (e) $[PPh_4][W^{V}(bdt)_3]$, (f) $[NEt_4][W^{V}(mdt)_3]$, (g) $[W^{VI}(bdt)_3]$, (h) $[W^{VI}(mdt)_3]$, (i) $[W^{VI}(pdt)_3]$.

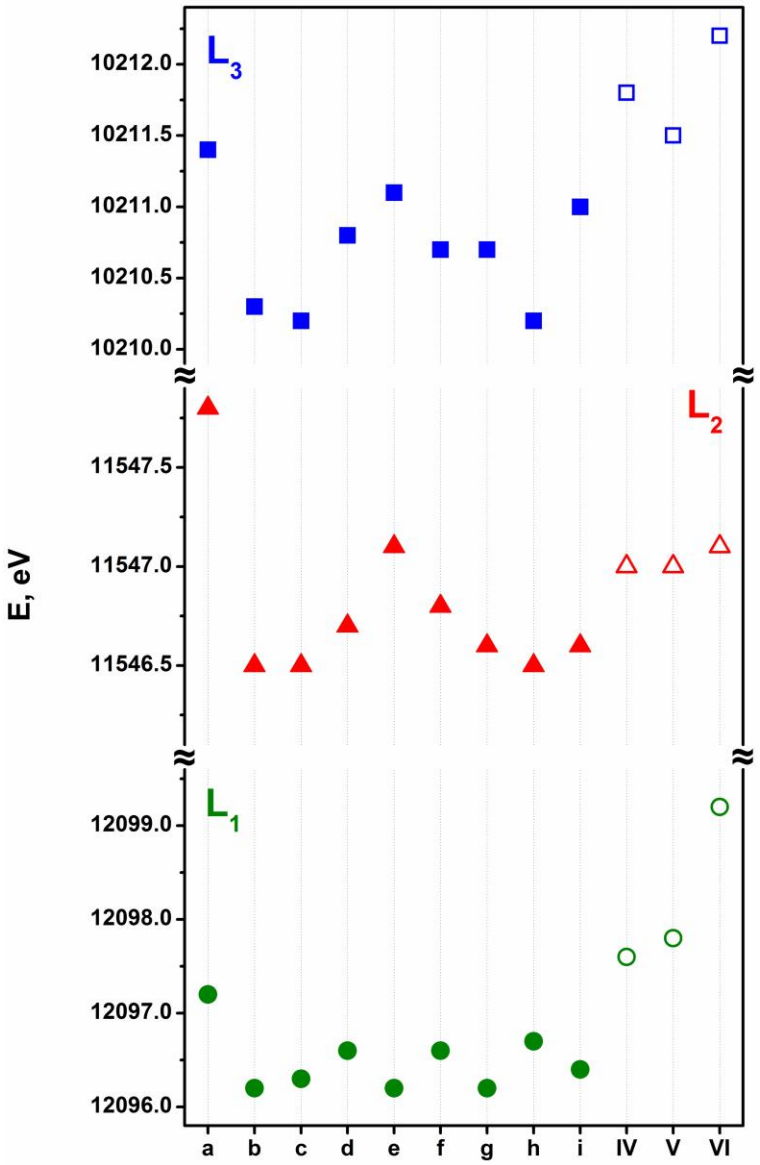

Figure S11. Comparison of the L_3- (■), L_2- (▲) and L_1-edge (●) energies of (a) $[PPh_4]_2[W^{IV}(mnt)_3]$, (b) $[PPh_4]_2[W^{IV}(bdt)_3]$, (c) $[NEt_4]_2[W^{IV}(bdt)_3]$, (d) $[NEt_4]_2[W^{IV}(mdt)_3]$, (e) $[PPh_4][W^{V}(bdt)_3]$, (f) $[NEt_4][W^{V}(mdt)_3]$, (g) $[W^{VI}(bdt)_3]$, (h) $[W^{VI}(mdt)_3]$, (i) $[W^{VI}(pdt)_3]$, with calibrants (IV) $[W^{IV}Cl_4(PMePh_2)_2]$, (IV) $[W^{V}(NPh)Cl_3(PMe_3)_2]$, (IV) $[W^{VI}Cl_6]$, represented by the open shapes.

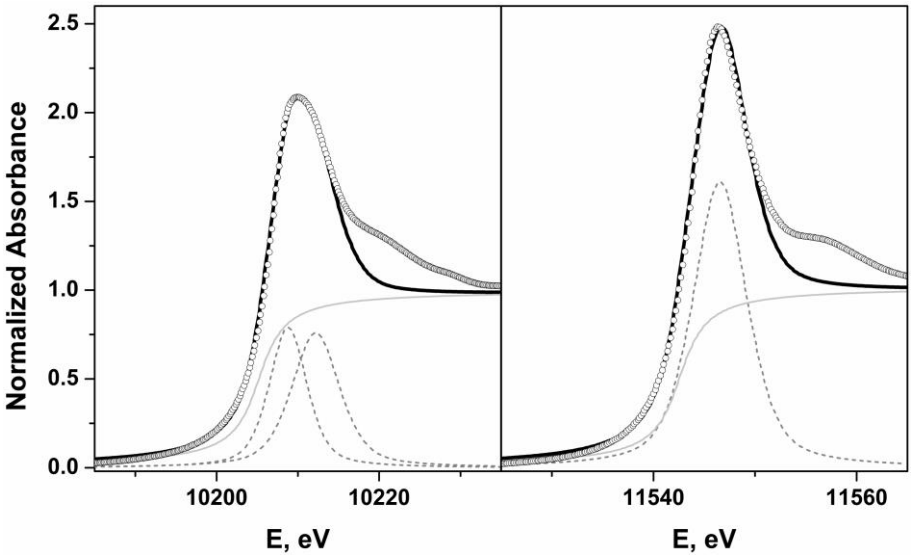

Figure S12. Pseudo-Voigt deconvolution of the W L_3-edge (left) and L_2-edge (right) spectra of W reference foil.

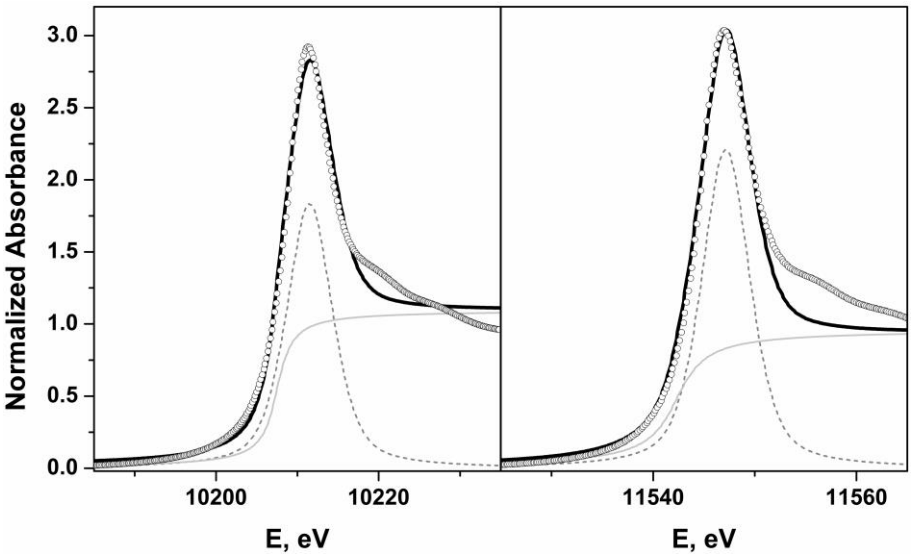

Figure S13. Pseudo-Voigt deconvolution of the W L_3-edge (left) and L_2-edge (right) spectra of $[W^0(PMe_3)_6]$.

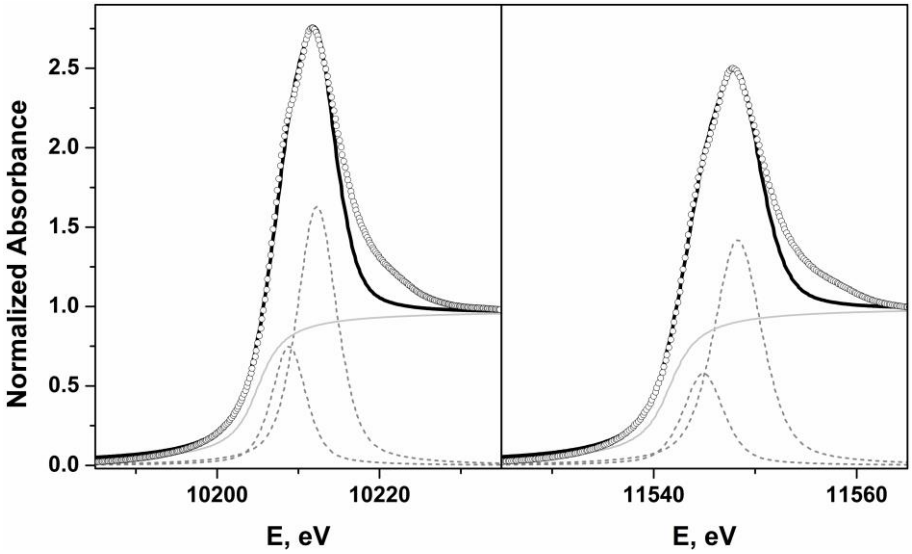

Figure S14. Pseudo-Voigt deconvolution of the W L_3-edge (left) and L_2-edge (right) spectra of $[W^{II}Cl_2(PMePh_2)_4]$.

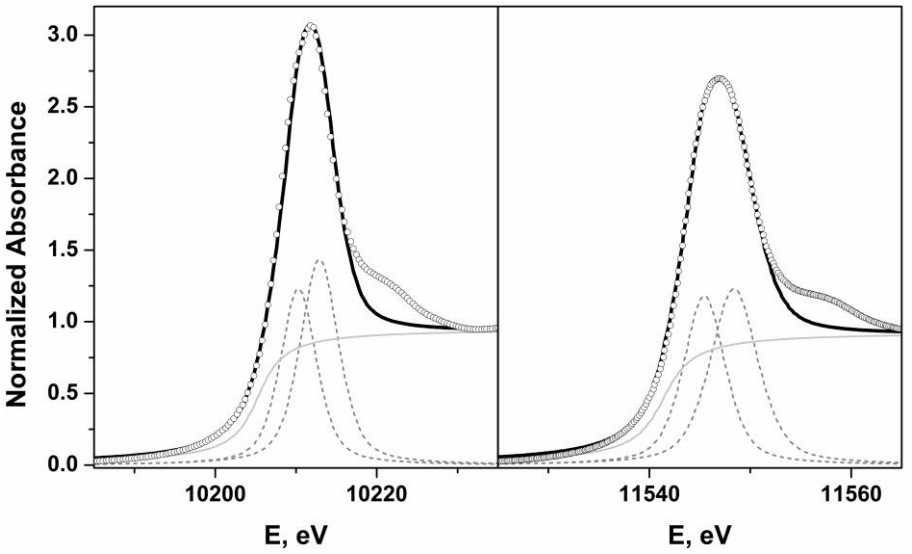

Figure S15. Pseudo-Voigt deconvolution of the W L_3-edge (left) and L_2-edge (right) spectra of $[W^{III}Cl_2(dppe)_2][PF_6]$.

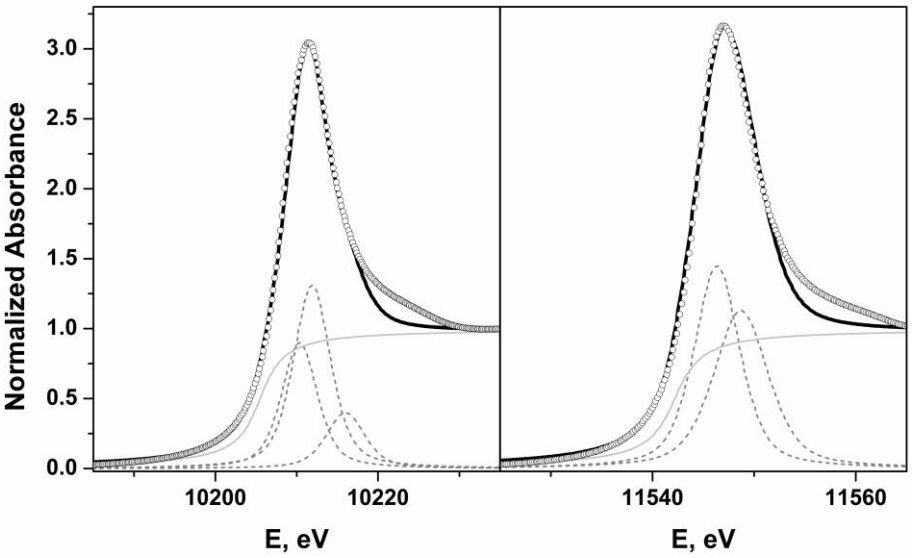

Figure S16. Pseudo-Voigt deconvolution of the W L_3-edge (left) and L_2-edge (right) spectra of $[W^{IV}Cl_4(PMePh_2)_2]$.

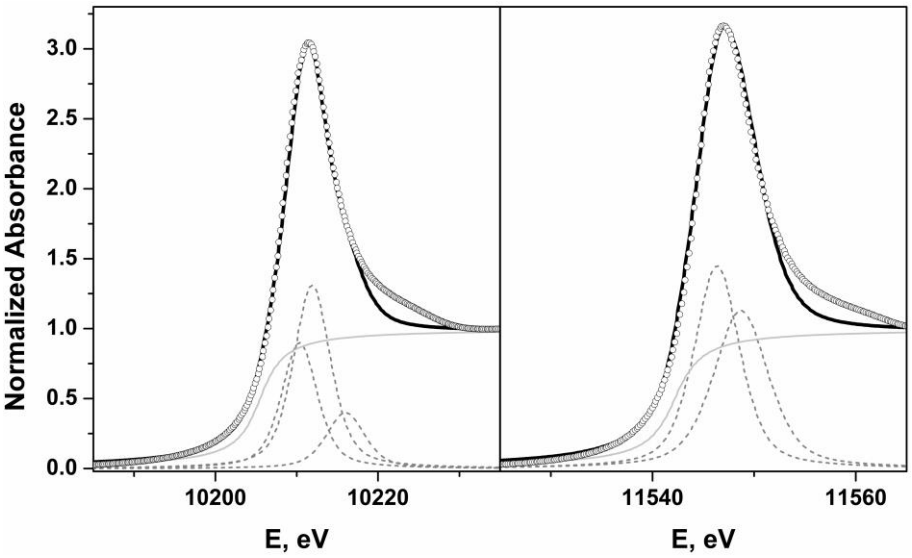

Figure S17. Pseudo-Voigt deconvolution of the W L_3-edge (left) and L_2-edge (right) spectra of $[W^{V}(NPh)Cl_3(PMe_3)_2]$.

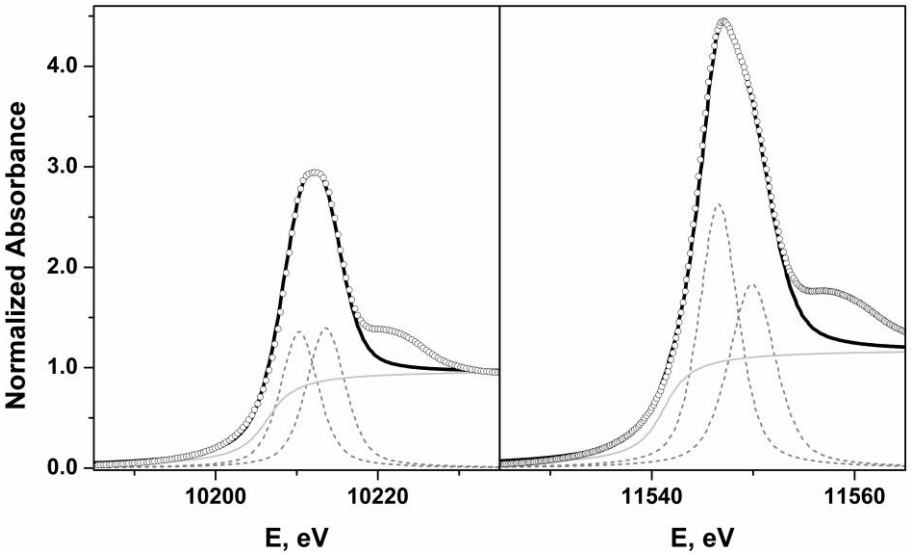

Figure S18. Pseudo-Voigt deconvolution of the W L_3-edge (left) and L_2-edge (right) spectra of $[W^{VI}Cl_6]$.

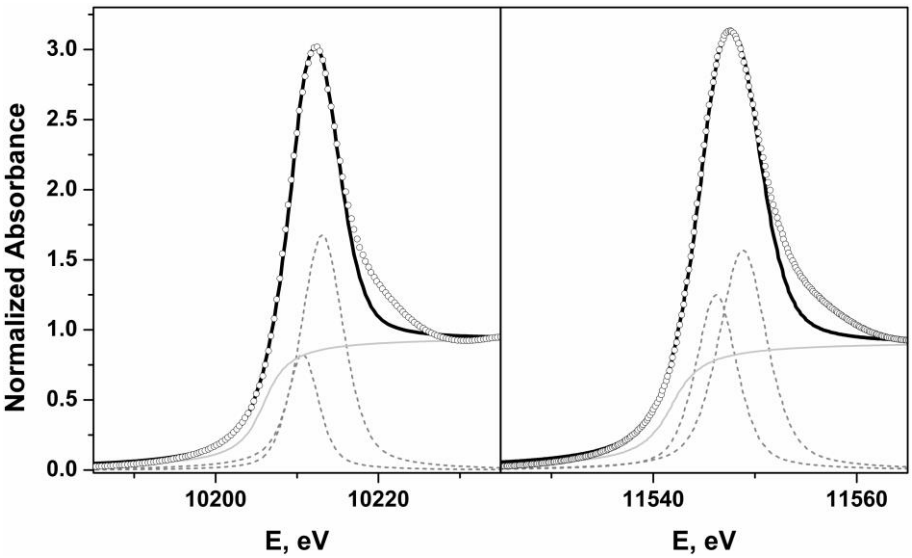

Figure S19. Pseudo-Voigt deconvolution of the W L_3-edge (left) and L_2-edge (right) spectra of $[W^{VI}(xylidene)_3]$.

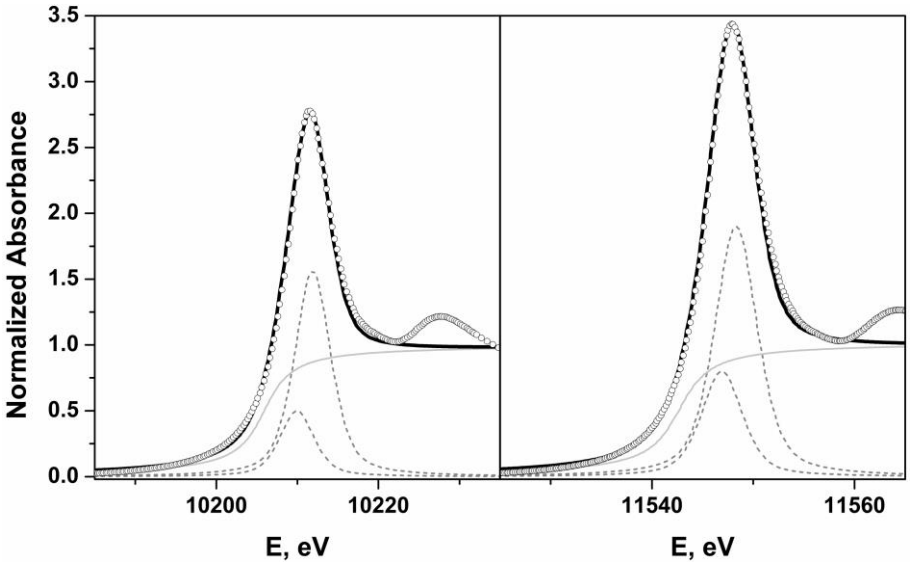

Figure S20. Pseudo-Voigt deconvolution of the W L_3-edge (left) and L_2-edge (right) spectra of $[W^0(CO)_6]$.

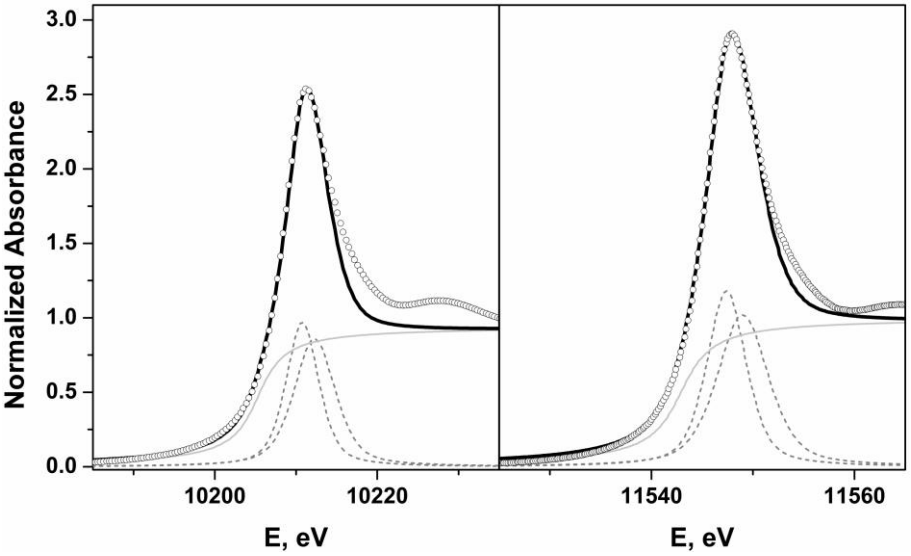

Figure S21. Pseudo-Voigt deconvolution of the W L_3-edge (left) and L_2-edge (right) spectra of $[W^0(Me_2pipdt)(CO)_4]$.

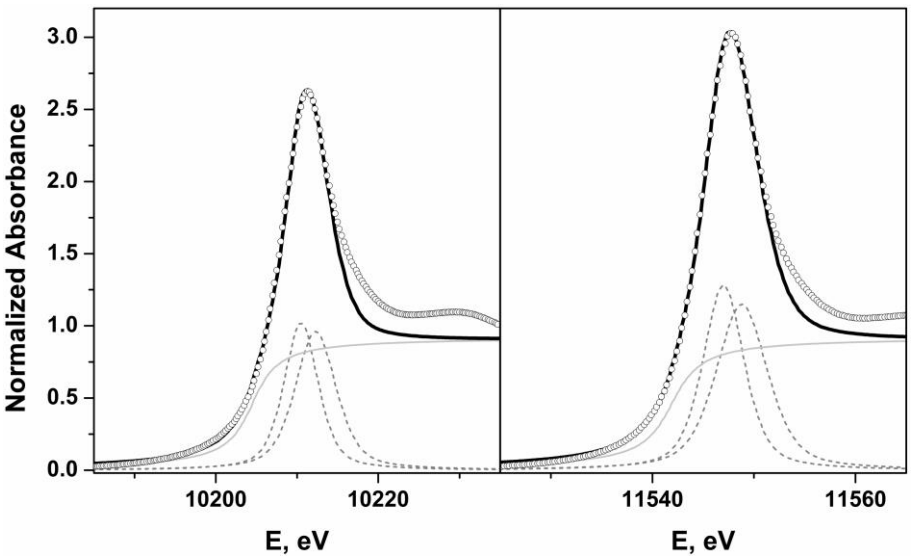

Figure S22. Pseudo-Voigt deconvolution of the W L_3-edge (left) and L_2-edge (right) spectra of $[W^{II}(mdt)(CO)_4]$.

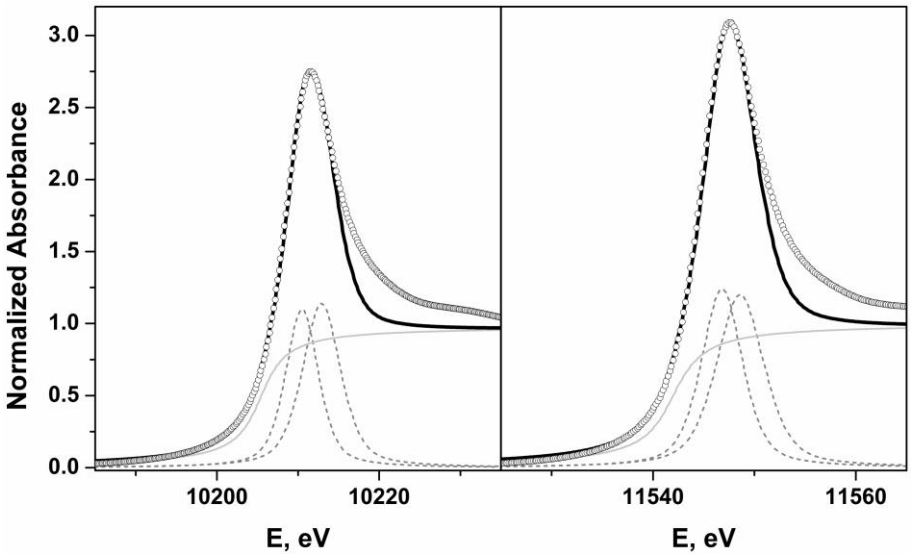

Figure S23. Pseudo-Voigt deconvolution of the W L_3-edge (left) and L_2-edge (right) spectra of $[W^{II}(mdt)(CO)_2(PMe_3)_2]$.

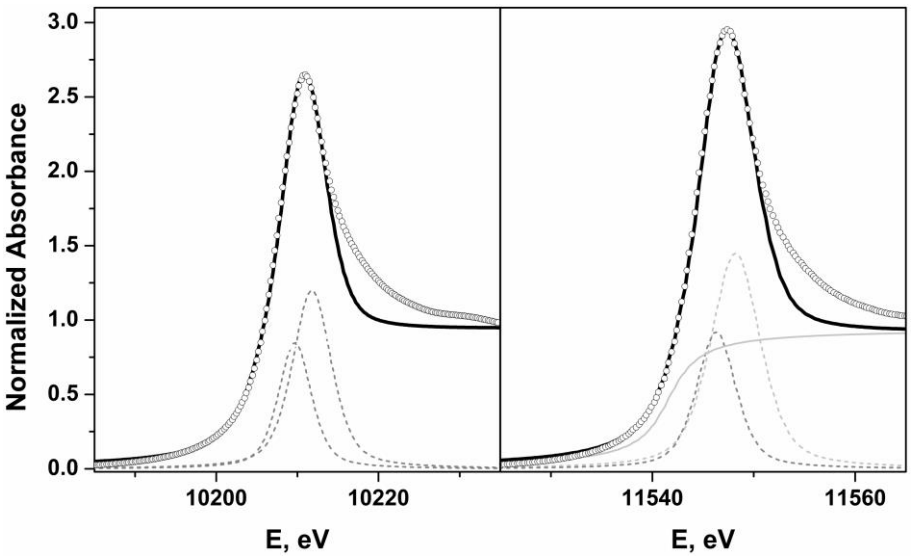

Figure S24. Pseudo-Voigt deconvolution of the W L_3-edge (left) and L_2-edge (right) spectra of $[W^{IV}(mdt)_2(CO)_2]$.

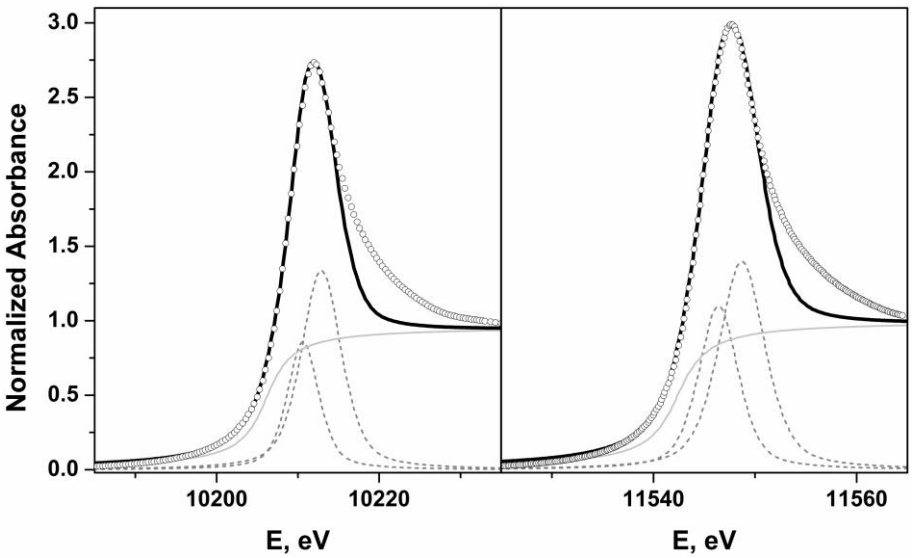

Figure S25. Pseudo-Voigt deconvolution of the W L_3-edge (left) and L_2-edge (right) spectra of $[W^{IV}(mdt)_2(CO)(PMe_3)]$.

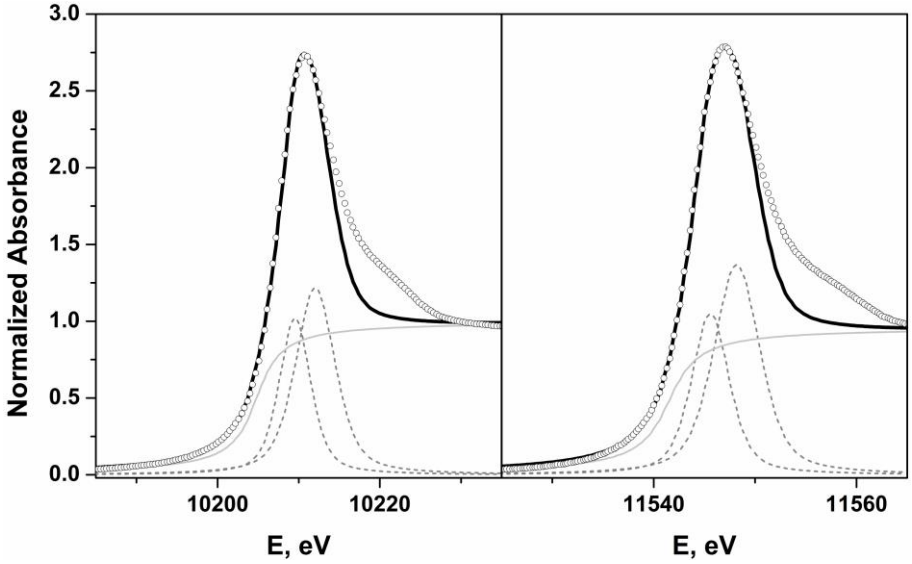

Figure S26. Pseudo-Voigt deconvolution of the W L_3-edge (left) and L_2-edge (right) spectra of $[W^{IV}(mdt)_2(PMe_3)_2]$.

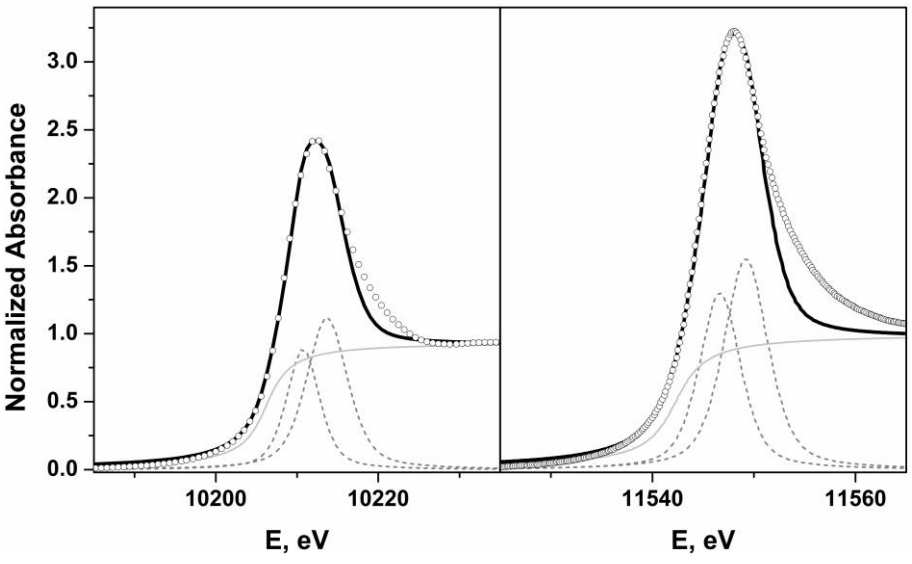

Figure S27. Pseudo-Voigt deconvolution of the W L_3-edge (left) and L_2-edge (right) spectra of $[W^{IV}(mdt)_2(CN^tBu)_2]$.

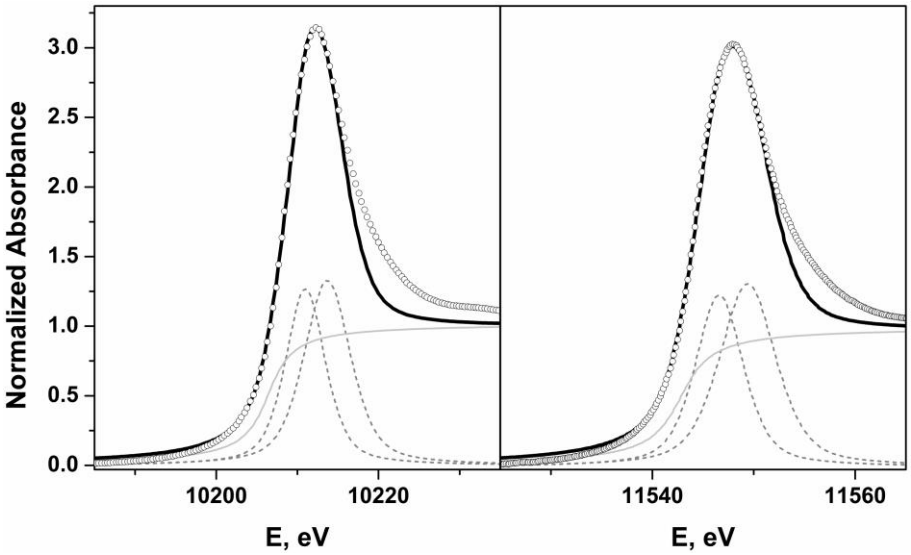

Figure S28. Pseudo-Voigt deconvolution of the W L_3-edge (left) and L_2-edge (right) spectra of $[NEt_4]_2[W^{IV}(mdt)_2(CN)_2]$.

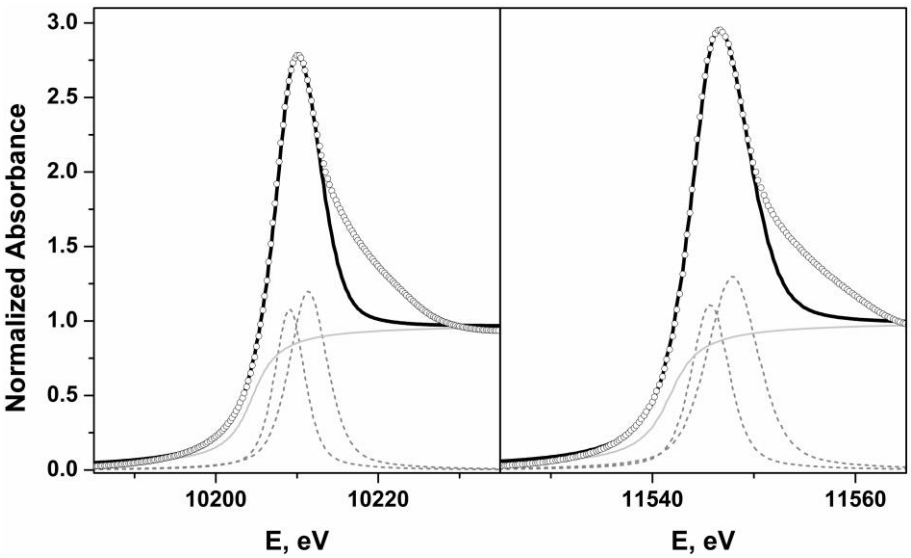

Figure S29. Pseudo-Voigt deconvolution of the W L_3-edge (left) and L_2-edge (right) spectra of $[PPh_4]_2[W^{IV}(mnt)_3]$.

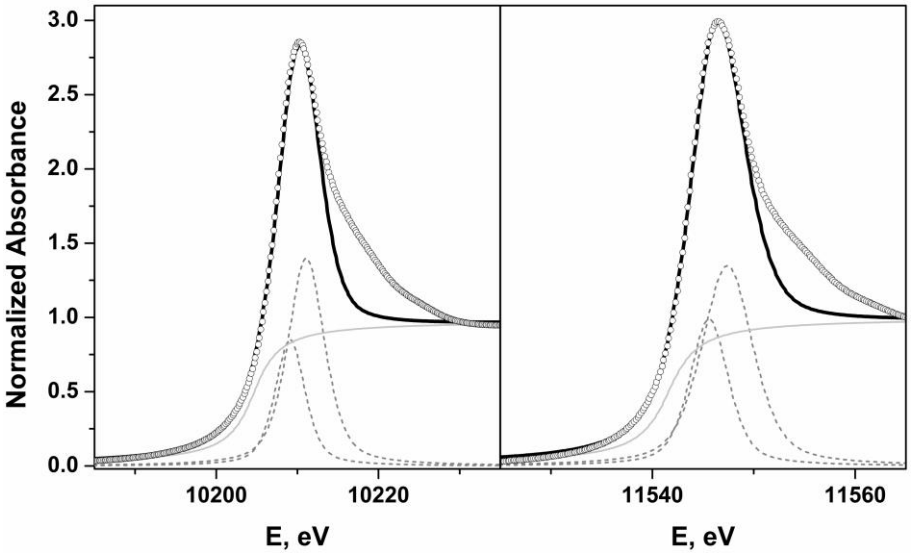

Figure S30. Pseudo-Voigt deconvolution of the W L_3-edge (left) and L_2-edge (right) spectra of $[NEt_4]_2[W^{IV}(bdt)_3]$.

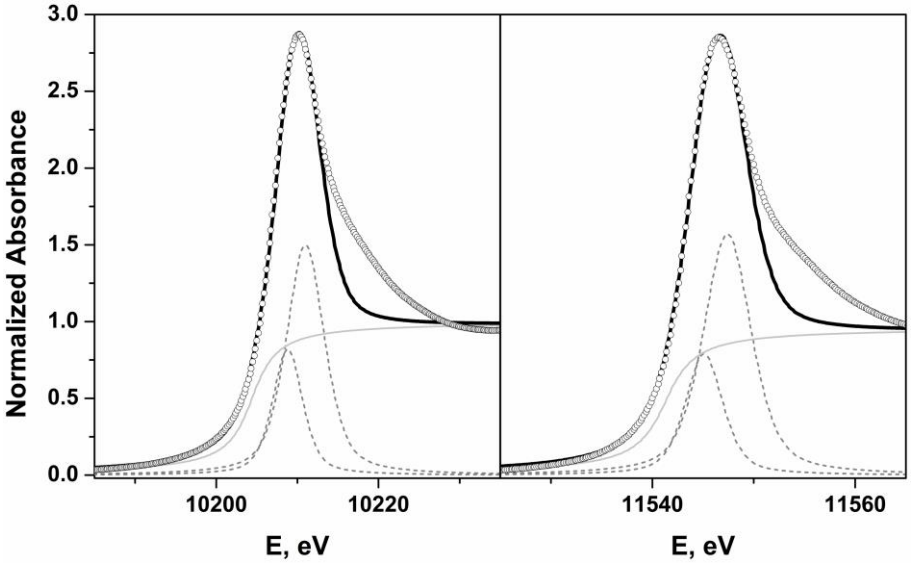

Figure S31. Pseudo-Voigt deconvolution of the W L_3-edge (left) and L_2-edge (right) spectra of $[PPh_4]_2[W^{IV}(bdt)_3]$.

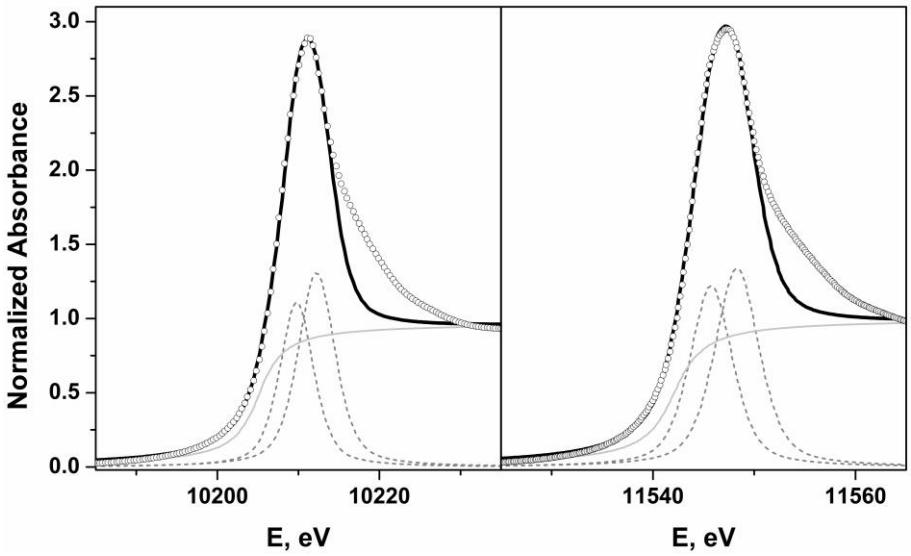

Figure S32. Pseudo-Voigt deconvolution of the W L_3-edge (left) and L_2-edge (right) spectra of $[PPh_4][W^{V}(bdt)_3]$.

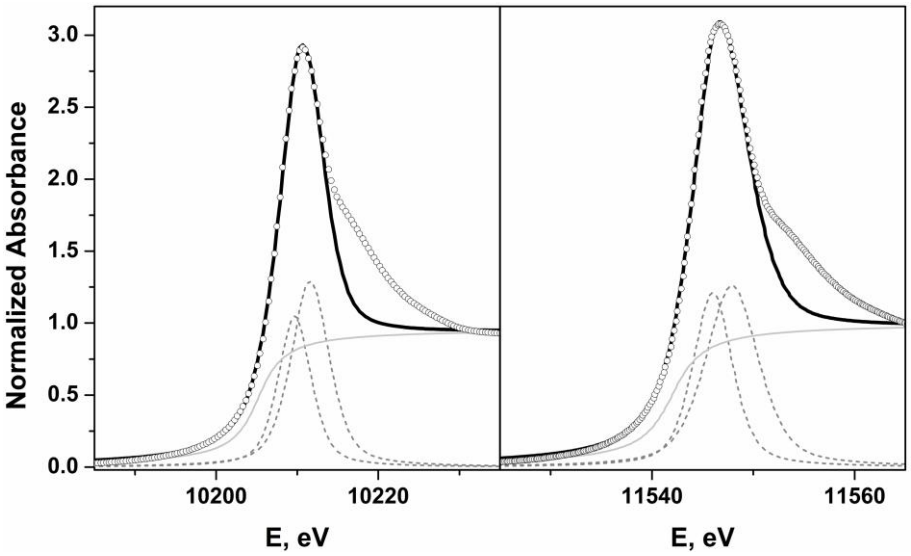

Figure S33. Pseudo-Voigt deconvolution of the W L_3-edge (left) and L_2-edge (right) spectra of $[W^{VI}(bdt)_3]$.

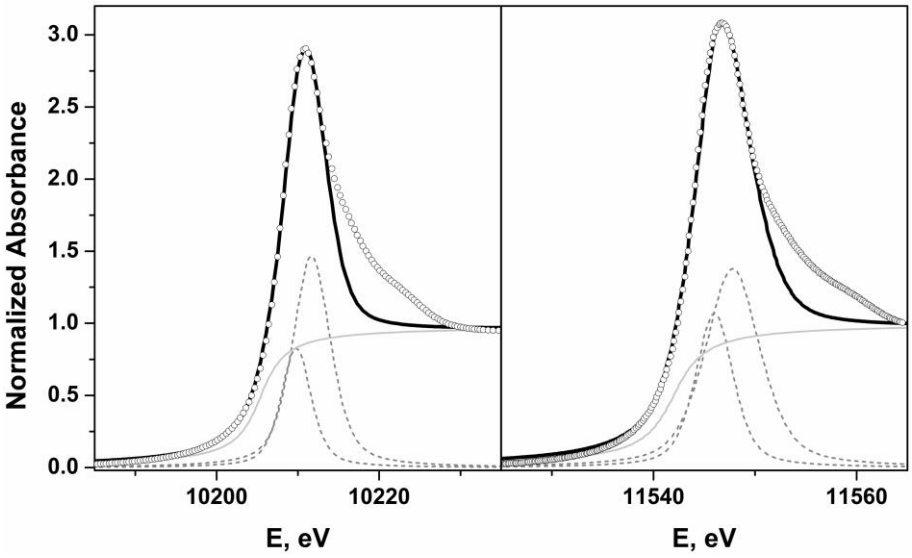

Figure S34. Pseudo-Voigt deconvolution of the W L_3-edge (left) and L_2-edge (right) spectra of $[NEt_4]_2[W^{IV}(mdt)_3]$.

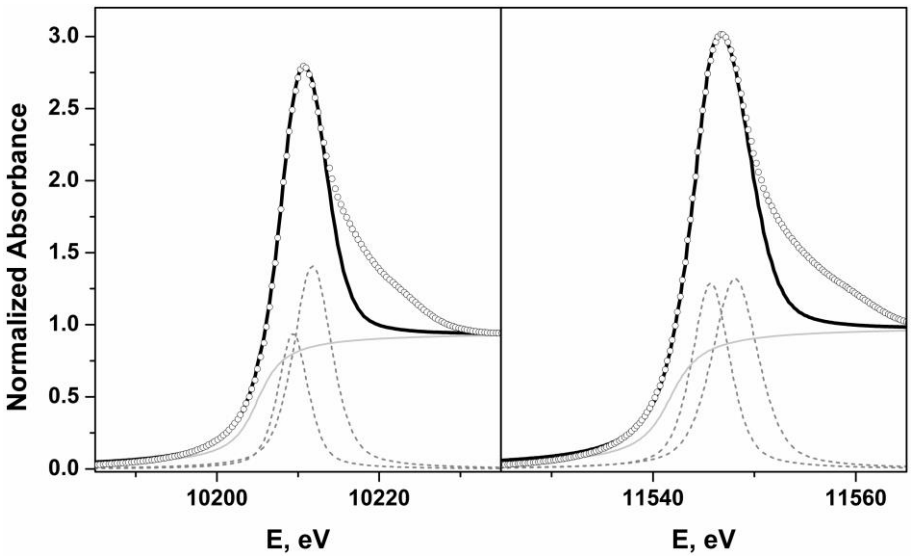

Figure S35. Pseudo-Voigt deconvolution of the W L_3-edge (left) and L_2-edge (right) spectra of $[NEt_4][W^{V}(mdt)_3]$.

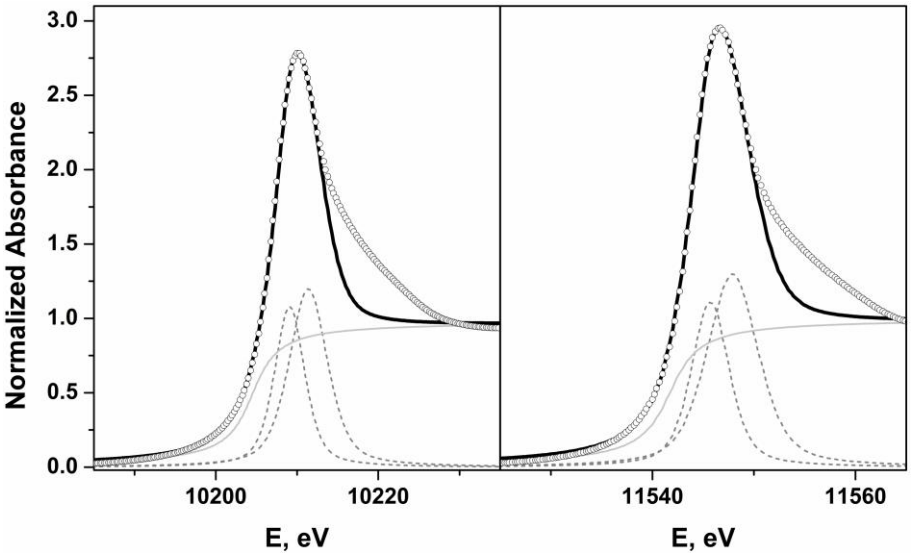

Figure S36. Pseudo-Voigt deconvolution of the W L_3-edge (left) and L_2-edge (right) spectra of $[W^{VI}(mdt)_3]$.

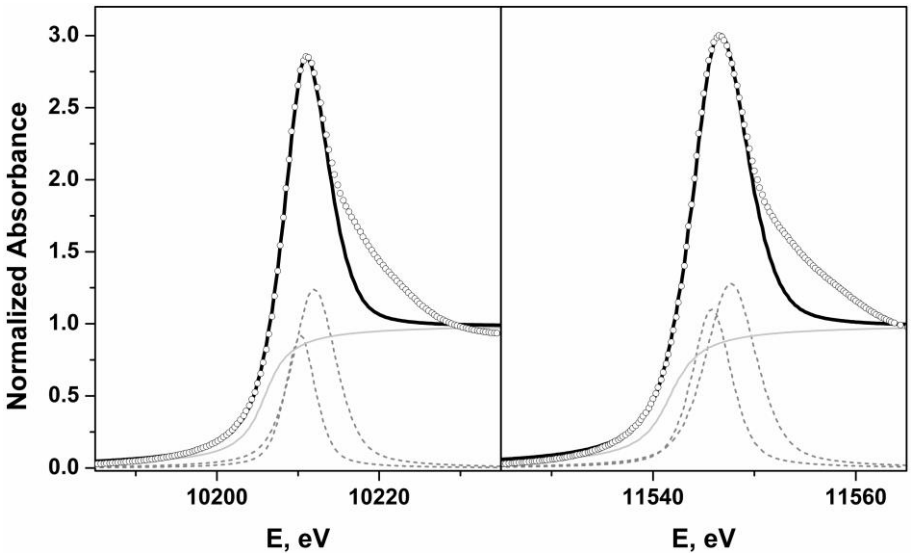

Figure S37. Pseudo-Voigt deconvolution of the W L_3-edge (left) and L_2-edge (right) spectra of $[W^{VI}(pdt)_3]$.

Table S2. L_3- and L_2-edge White-Line Energies (eV) and EBR for Complexes

Compound	L_3	L_2	EBR
$[W^{VI}(xylidene)_3]$	10212.4	11547.6	0.490
$[W^{0}(CO)_6]$	10211.6	11547.9	0.447
$[W^{0}(Me_2pipdt)(CO)_4]$	10211.2	11547.9	0.459
$[W^{II}(mdt)(CO)_4]$	10211.3	11547.7	0.454
$[W^{II}(mdt)(CO)_2(PMe_3)_2]$	10211.5	11547.6	0.479
$[W^{IV}(mdt)_2(CO)_2]$	10211.0	11547.4	0.463
$[W^{IV}(mdt)_2(CO)(PMe_3)]$	10212.0	11547.6	0.482
$[W^{IV}(mdt)_2(PMe_3)_2]$	10210.7	11547.0	0.495
$[W^{IV}(mdt)_2(CN^tBu)_2]$	10212.3	11548.0	0.435
$[NEt_4]_2[W^{IV}(mdt)_2(CN)_2]$	10212.3	11547.9	0.514
$[PPh_4]_2[W^{IV}(mnt)_3]$	10211.4	11547.8	0.504
$[PPh_4]_2[W^{IV}(bdt)_3]$	10210.2	11546.5	0.495
$[NEt_4]_2[W^{IV}(bdt)_3]$	10210.2	11546.5	0.474
$[NEt_4]_2[W^{IV}(mdt)_3]$	10210.8	11546.7	0.464
$[PPh_4][W^{V}(bdt)_3]$	10211.1	11547.1	0.491
$[NEt_4][W^{V}(mdt)_3]$	10210.7	11546.8	0.484
$[W^{VI}(bdt)_3]$	10210.7	11546.6	0.478
$[W^{VI}(mdt)_3]$	10210.2	11546.5	0.475
$[W^{VI}(pdt)_3]$	10211.0	11546.6	0.485

Table S3. Optimized Coordinations for $[W(PH_3)_6]$

74	-0.013831	0.000548	0.000446
15	1.440206	0.517995	-1.838415
1	2.884958	0.436996	-1.697048
1	1.415745	-0.214967	-3.092269
1	1.468824	1.824282	-2.473468
15	-1.403326	-1.304880	-1.440822
1	-0.836626	-2.245190	-2.392585
1	-2.386701	-2.239047	-0.919210
1	-2.308300	-0.693409	-2.399058
15	-1.326853	1.941618	-0.469506
1	-0.707569	3.224460	-0.755231
1	-2.242334	1.994660	-1.596549
1	-2.278503	2.477994	0.488889
15	-1.431017	-0.527154	1.850856
1	-0.885512	-0.935769	3.133811
1	-2.353841	0.442872	2.415518
1	-2.405416	-1.603332	1.785247
15	1.345167	-1.923253	0.464649
1	2.796163	-1.831080	0.462199
1	1.286749	-2.645483	1.723705
1	1.313451	-3.122920	-0.353967
15	1.415285	1.294067	1.432014
1	2.861831	1.165959	1.360315
1	1.436208	2.746629	1.414209
1	1.372463	1.200861	2.880885

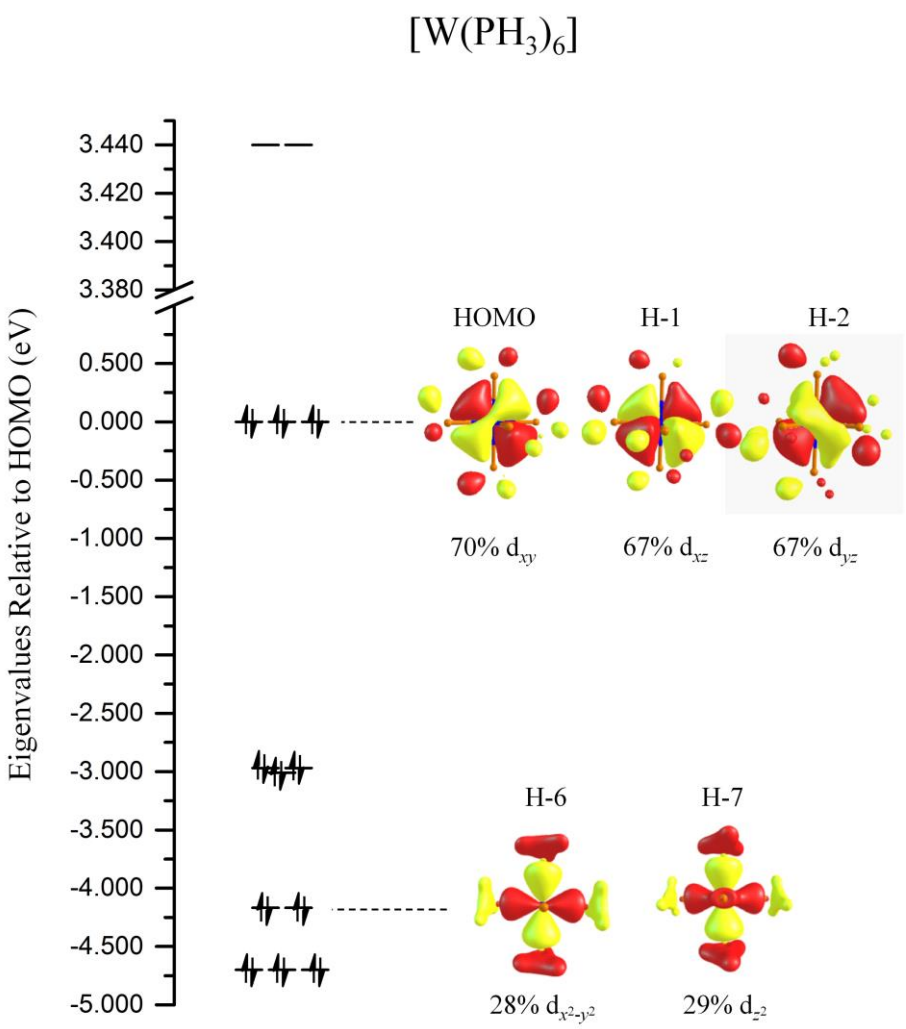

Figure S38. MO energy level diagram for $[W(PH_3)_6]$. Contour levels for the orbital images are drawn at the 0.05 level.

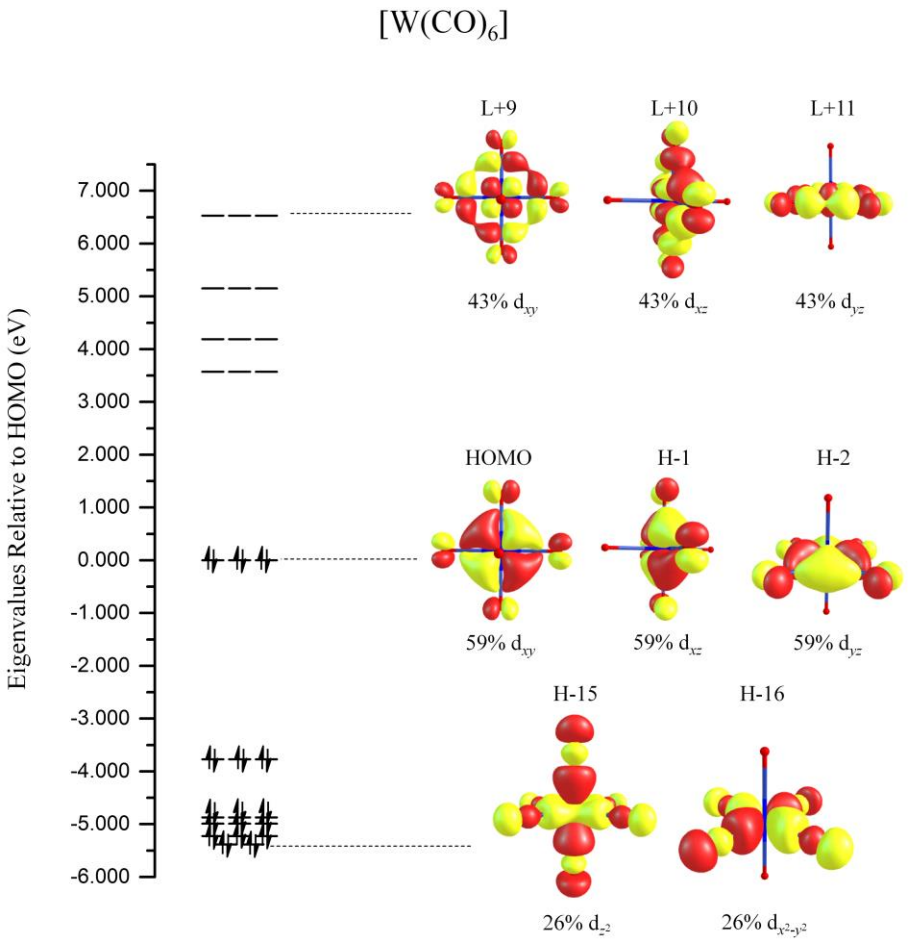

Figure S39. MO energy level diagram for $[W(CO)_6]$. Contour levels for the orbital images are drawn at the 0.05 level.

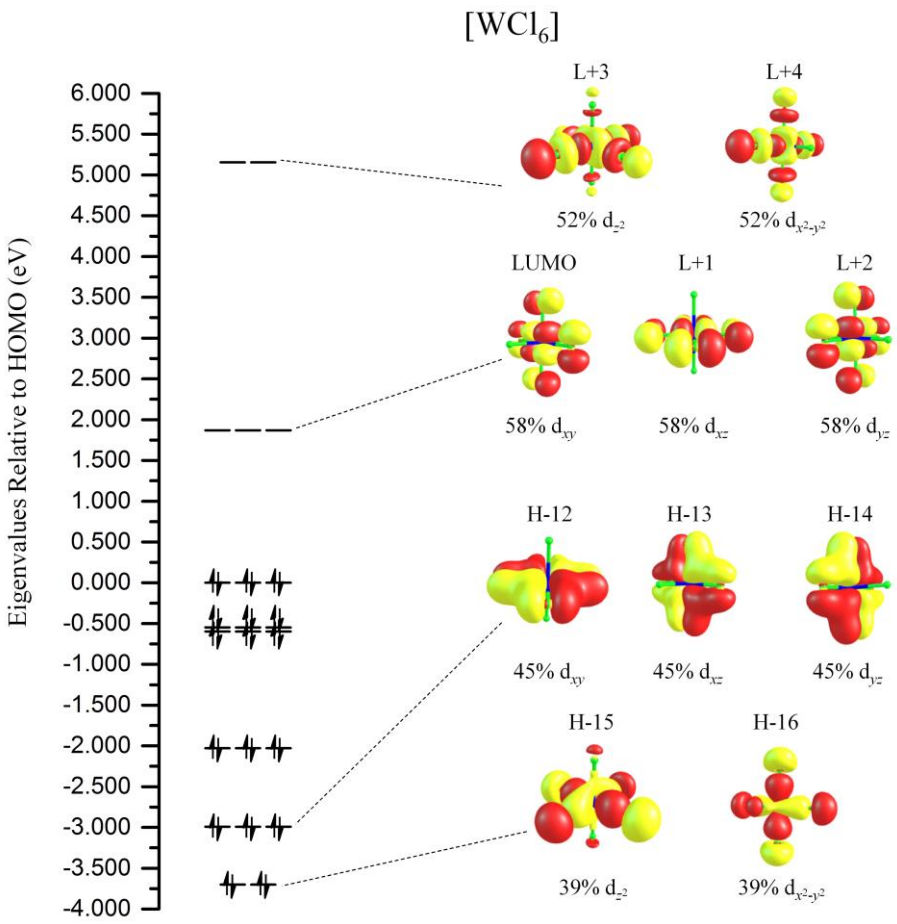

Figure S40. MO energy level diagram for $[WCl_6]$. Contour levels for the orbital images are drawn at the 0.05 level.

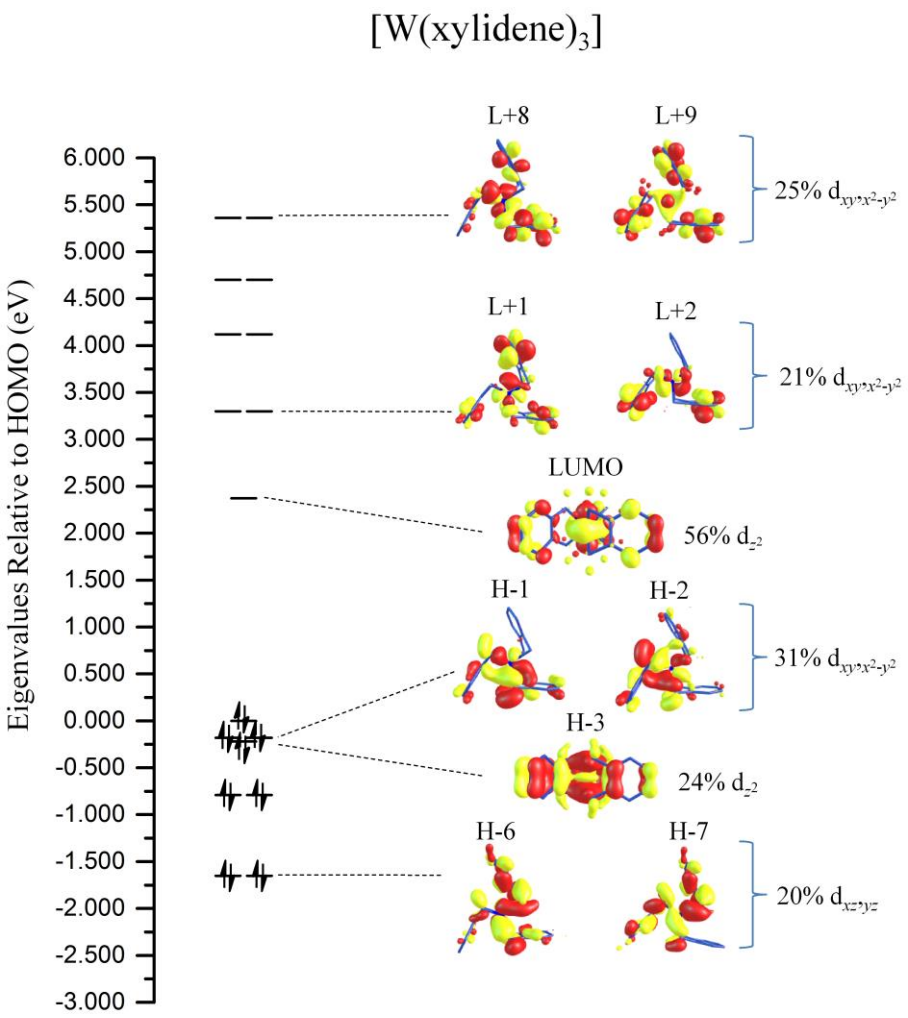

Figure S41. MO energy level diagram for [W(xylidene)$_3$]. Contour levels for the orbital images are drawn at the 0.05 level.

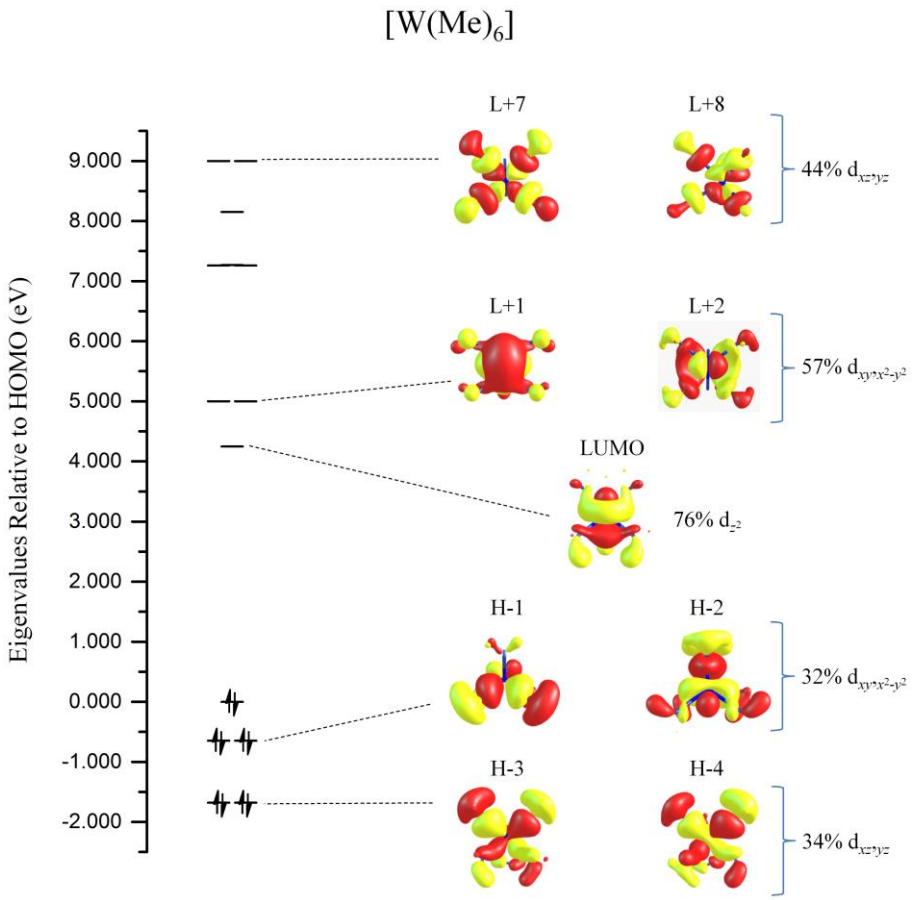

Figure S42. MO energy level diagram for $[W(Me)_6]$. Contour levels for the orbital images are drawn at the 0.05 level.

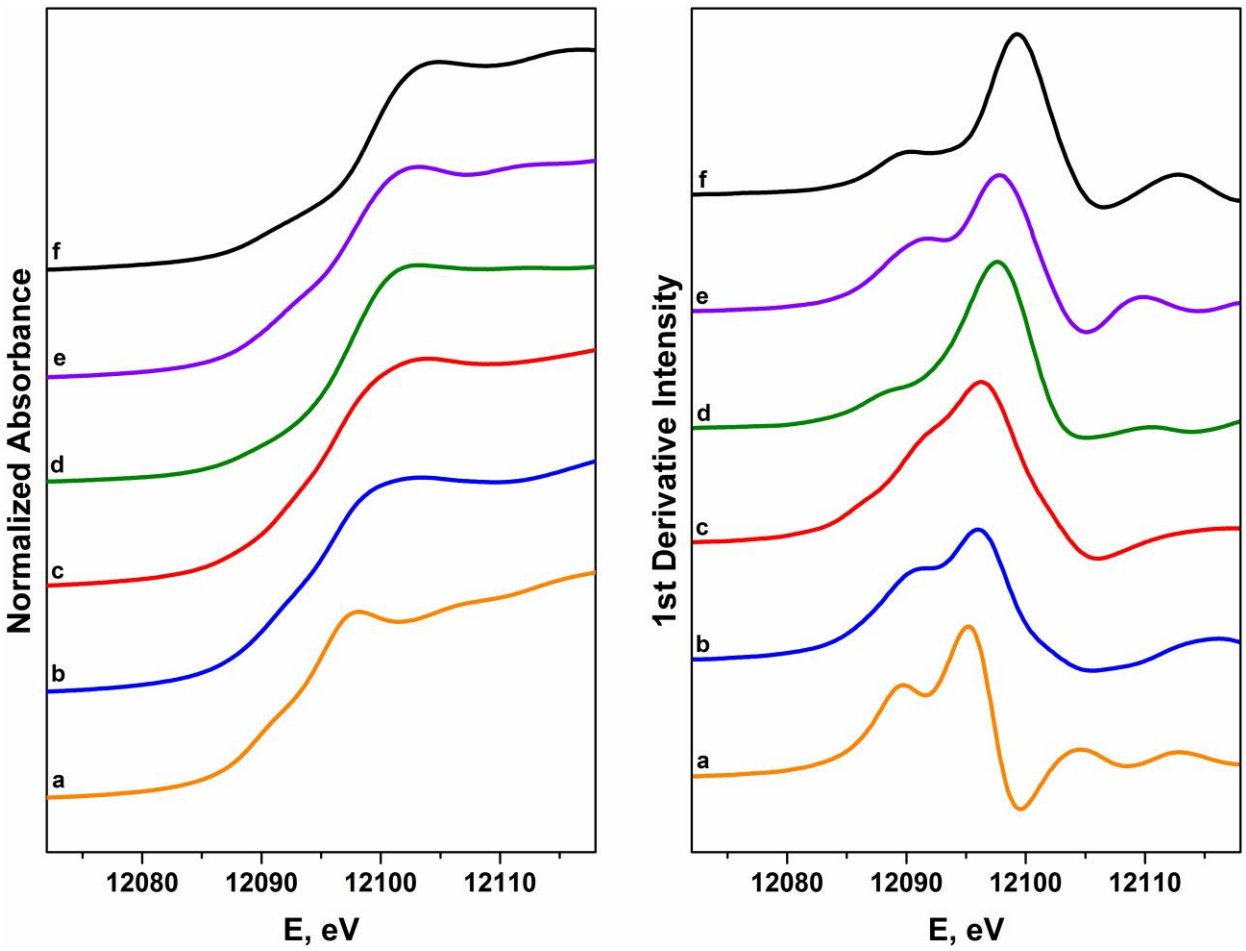

Figure S43. Comparison of the L_1-edge (panel A) and FFT smoothed first derivative (panel B) X-ray absorption spectra of (a) $[W^0(PMe_3)_6]$, (b) $[W^{II}Cl_2(PMePh_2)_4]$, (c) $[W^{III}Cl_2(dppe)_2][PF_6]$, (d) $[W^{IV}Cl_4(PMePh_2)_2]$, (e) $[W^{V}(NPh)Cl_3(PMe_3)_2]$, (f) $[W^{VI}Cl_6]$.

Table S4. W L_1-Pre- and Rising-Edge Energies (eV), W 6p% in LUMO and LUMO+1, and Trigonal Twist Angle, Θ (°)

	Pre-Edge	**Rising-Edge**	**W 6p**	**Θ**
$[NEt_4]_2[W(mdt)_3]$	12089.8	12096.6	3.5	2.4
$[NEt_4][W(mdt)_3]$	12089.8	12096.4	3.6	2.9
$[W(mdt)_3]$	12090.2	12096.5	4.5	0.7
$[NEt_4]_2[W(bdt)_3]$	12091.0	12096.3	3.4	1.9
$[PPh_4]_2[W(bdt)_3]$	12090.1	12096.2	1.9	23.0
$[PPh_4][W(bdt)_3]$	12090.0	12096.2	1.3	32.3
$[W(bdt)_3]$	12090.4	12096.2	3.9	0

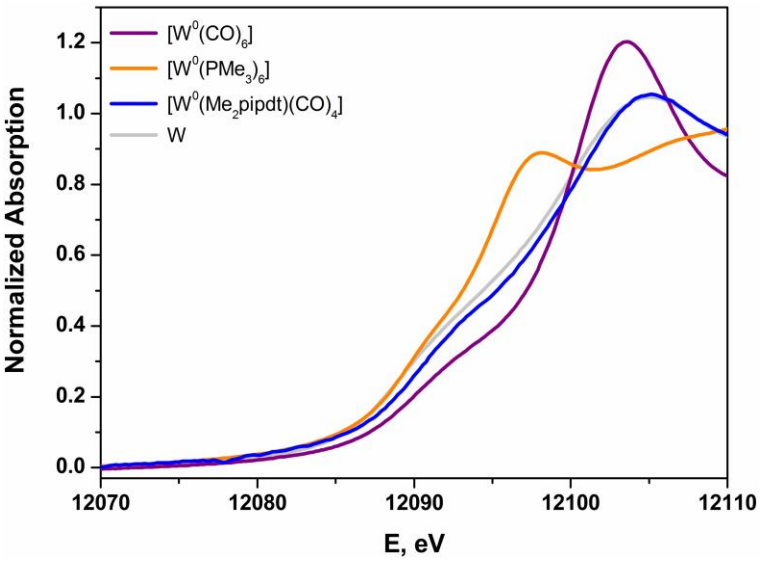

Figure S44. Overlay of the normalized W L_1-edge X-ray absorption spectra of $[W^0(CO)_6]$, $[W^0(PMe_3)_6]$, $[W^0(Me_2pipdt)(CO)_4]$, and W foil.

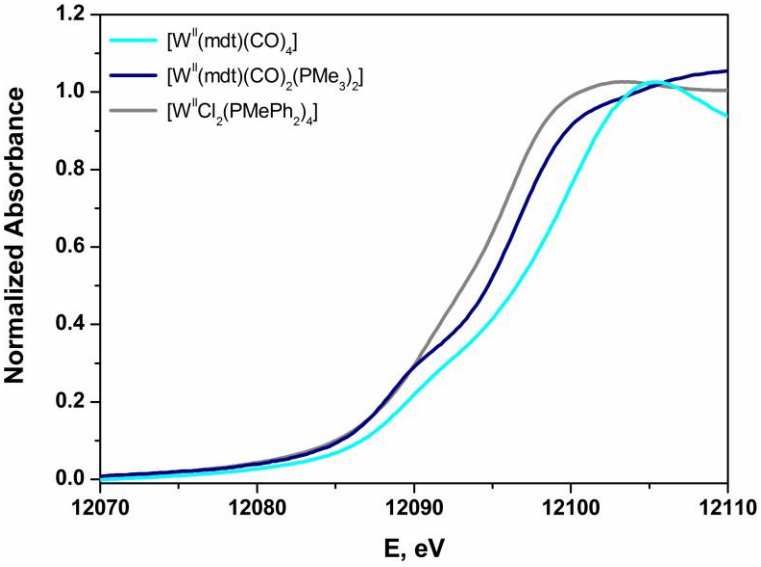

Figure S45. Overlay of the normalized W L_1-edge X-ray absorption spectra of formally W^{II} compounds $[W^{II}(mdt)(CO)_4]$, $[W^{II}(mdt)(CO)_2(PMe_3)_2]$, and $[W^{II}Cl_2(PMePh_2)_4]$.

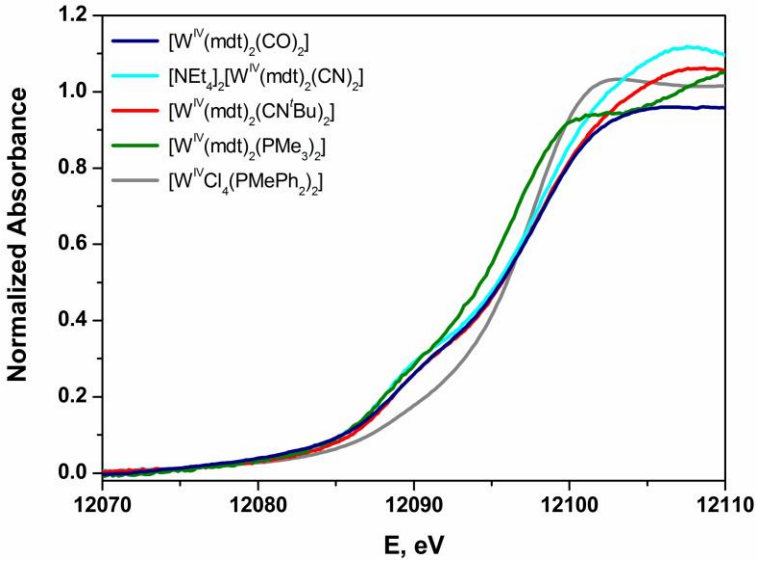

Figure S46. Overlay of the normalized W L_1-edge X-ray absorption spectra of formally W^{IV} compounds $[W^{IV}(mdt)_2(CO)_2]$, $[W^{IV}(mdt)_2(CO)(PMe_3)]$, $[W^{IV}(mdt)_2(PMe_3)_2]$, $[W^{IV}(mdt)_2(CN^tBu)_2]$, $[NEt_4]_2[W^{IV}(mdt)_2(CN)_2]$, and $[W^{IV}Cl_4(PMePh_2)_2]$.

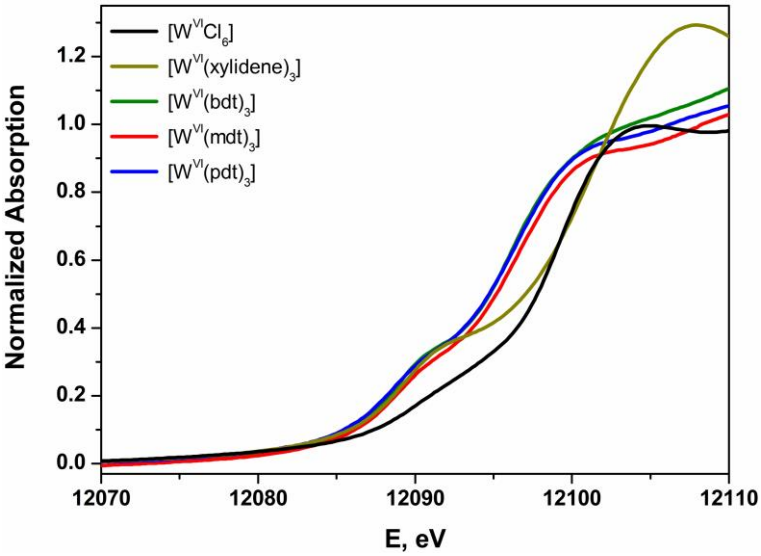

Figure S47. Overlay of the normalized W L_1-edge X-ray absorption spectra of formally W^{VI} compounds $[W^{VI}Cl_6]$, $[W^{VI}(xylidene)_3]$, $[W^{VI}(bdt)_3]$, $[W^{VI}(mdt)_3]$, and $[W^{VI}(pdt)_3]$.

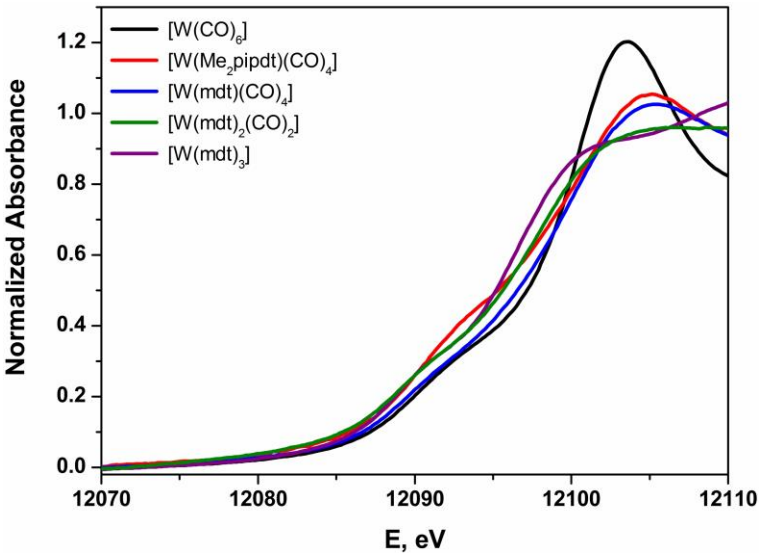

Figure S48. Overlay of the normalized W L_1-edge X-ray absorption spectra of $[W^0(CO)_6]$, $[W^0(Me_2pipdt)(CO)_4]$, $[W^{II}(mdt)(CO)_4]$, $[W^{IV}(mdt)_2(CO)_2]$, and $[W^{VI}(mdt)_3]$.

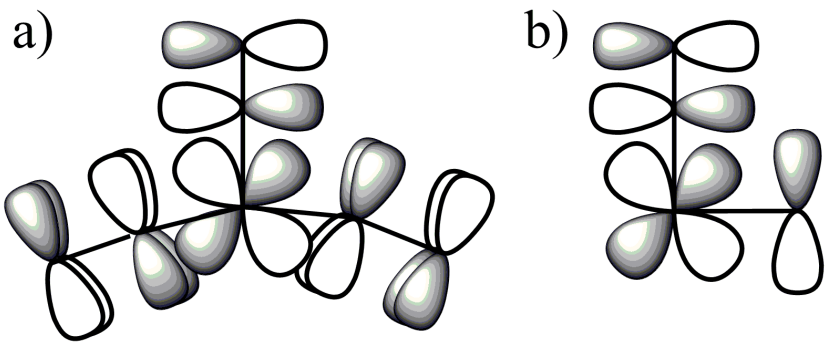

Figure S49. (a) Illustration of the HOMO-2 in $[W(mdt)_2(CO)_2]$, which is dithiolene-to-CO π* donating, via tungsten. (b) Illustration of the "synergistic" π-donating oxo and π-accepting carbonyl in *cis*-$W^{IV}O(CO)$ complexes, which is analogous to the MO shown in (a).

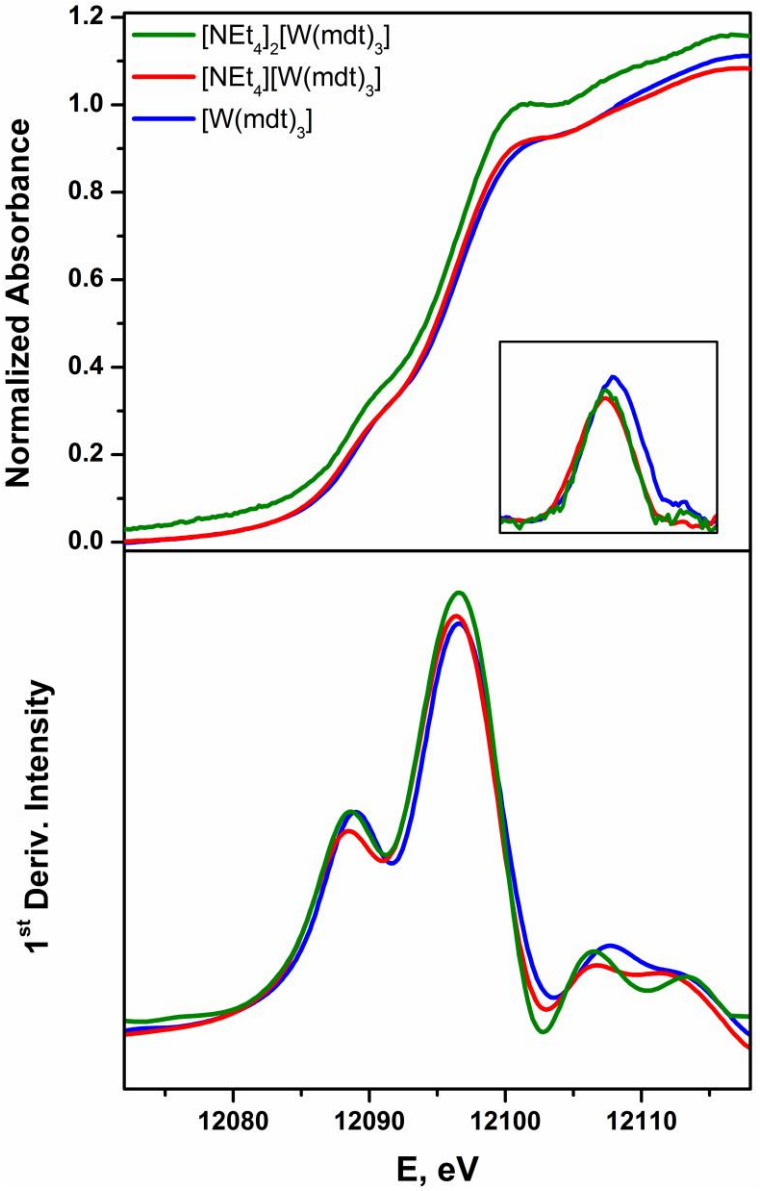

Figure S50. Overlay of the normalized W L_1-edge X-ray absorption (top) and first derivative spectra (bottom) of the series $[W(mdt)_3]^{0,1-,2-}$. Inset shows the relative intensity of the pre-edge peak at ~12090 eV.

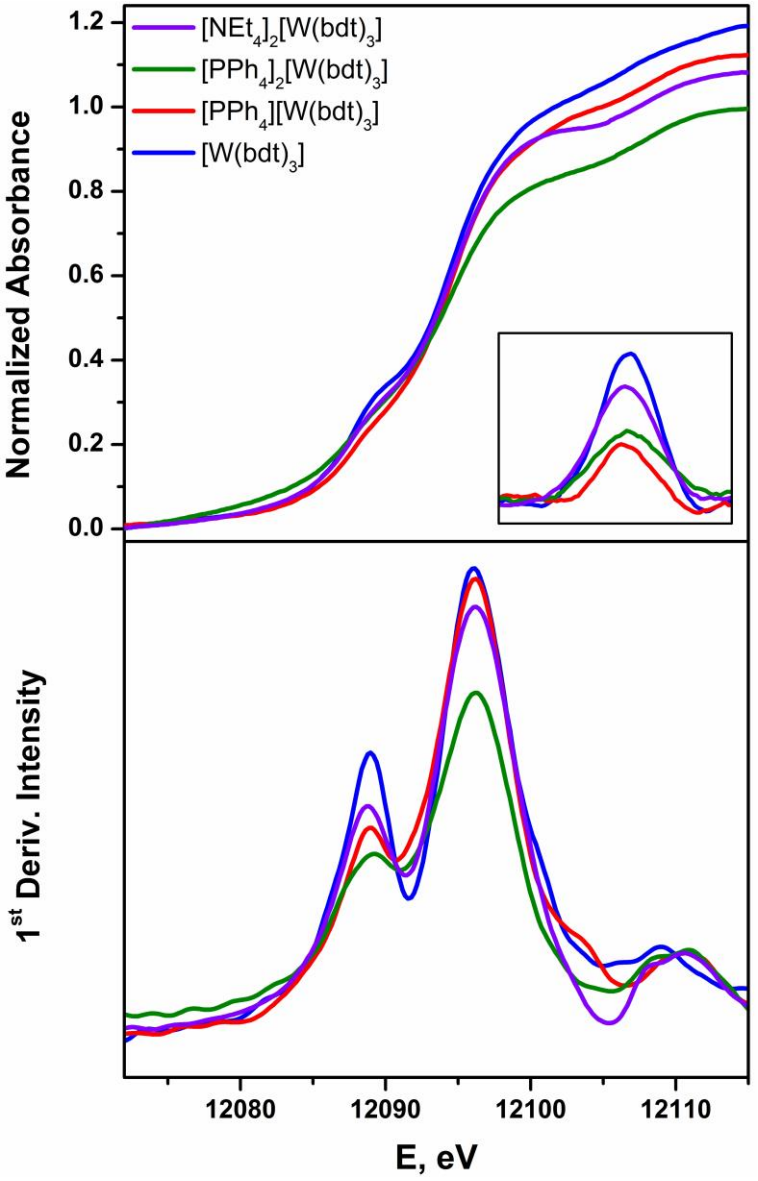

Figure S51. Overlay of the normalized W L_1-edge X-ray absorption (top) and first derivative spectra (bottom) of the series $[W(bdt)_3]^{0,1-,2-}$. Inset shows the relative intensity of the pre-edge peak at ~12090 eV.

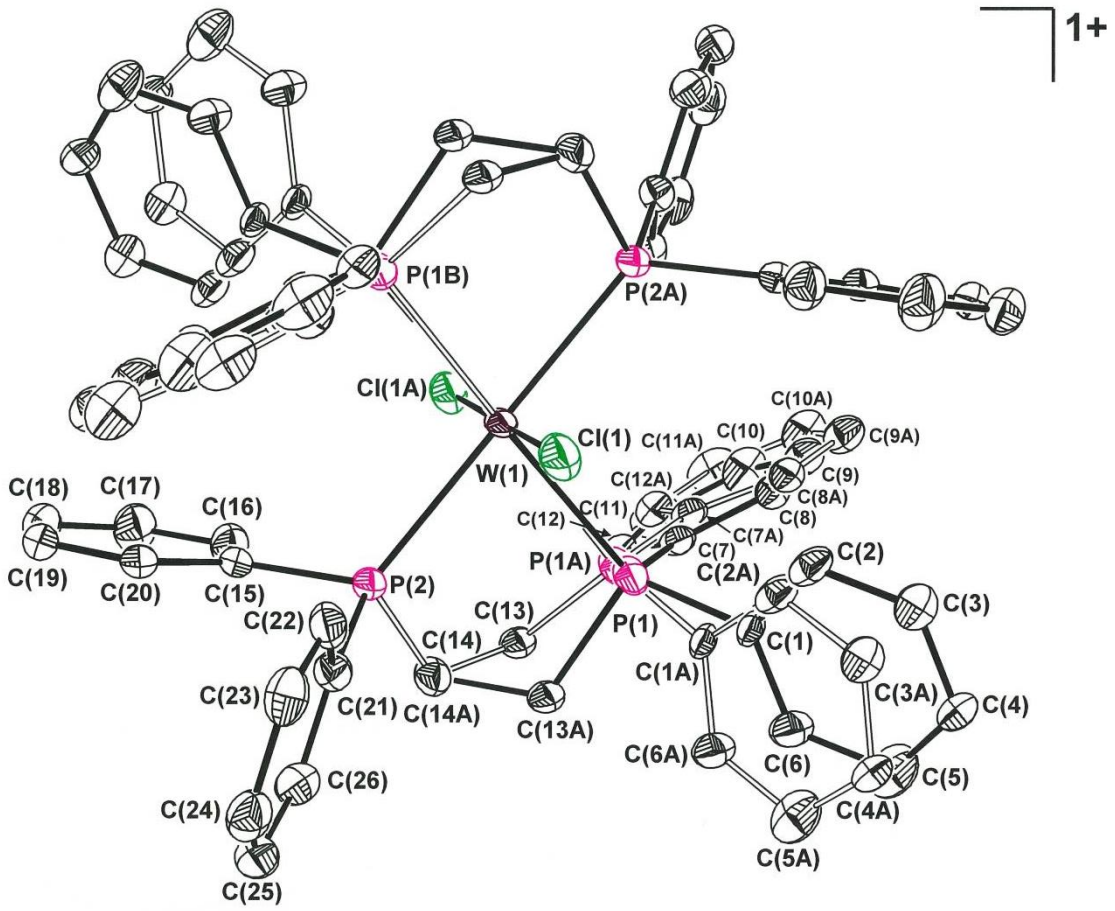

Figure S52. Thermal ellipsoid plot of cation 1 of $[W^{III}Cl_2(dppe)_2]^{1+}$ with complete atom labeling. The tungsten atom resides on an inversion center, which requires that only half of the cation be crystallographically unique. The ellipsoids are shown at the 50% probability level. Hydrogen atoms are omitted for clarity.

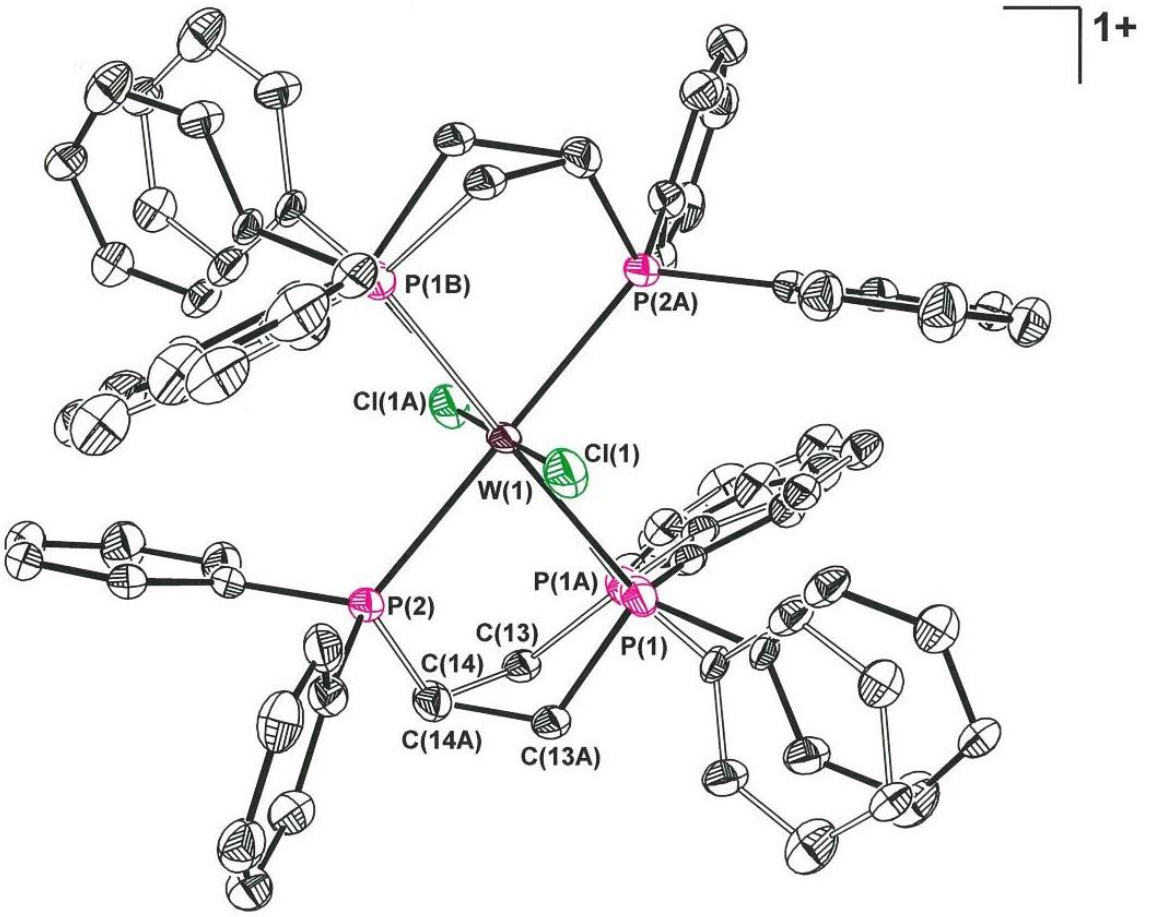

Figure S53. Thermal ellipsoid plot of cation 1 of $[W^{III}Cl_2(dppe)_2]^{1+}$ with partial atom labeling. The tungsten atom resides on an inversion center, which requires that only half of the cation be crystallographically unique. The ellipsoids are shown at the 50% probability level. Hydrogen atoms are omitted for clarity.

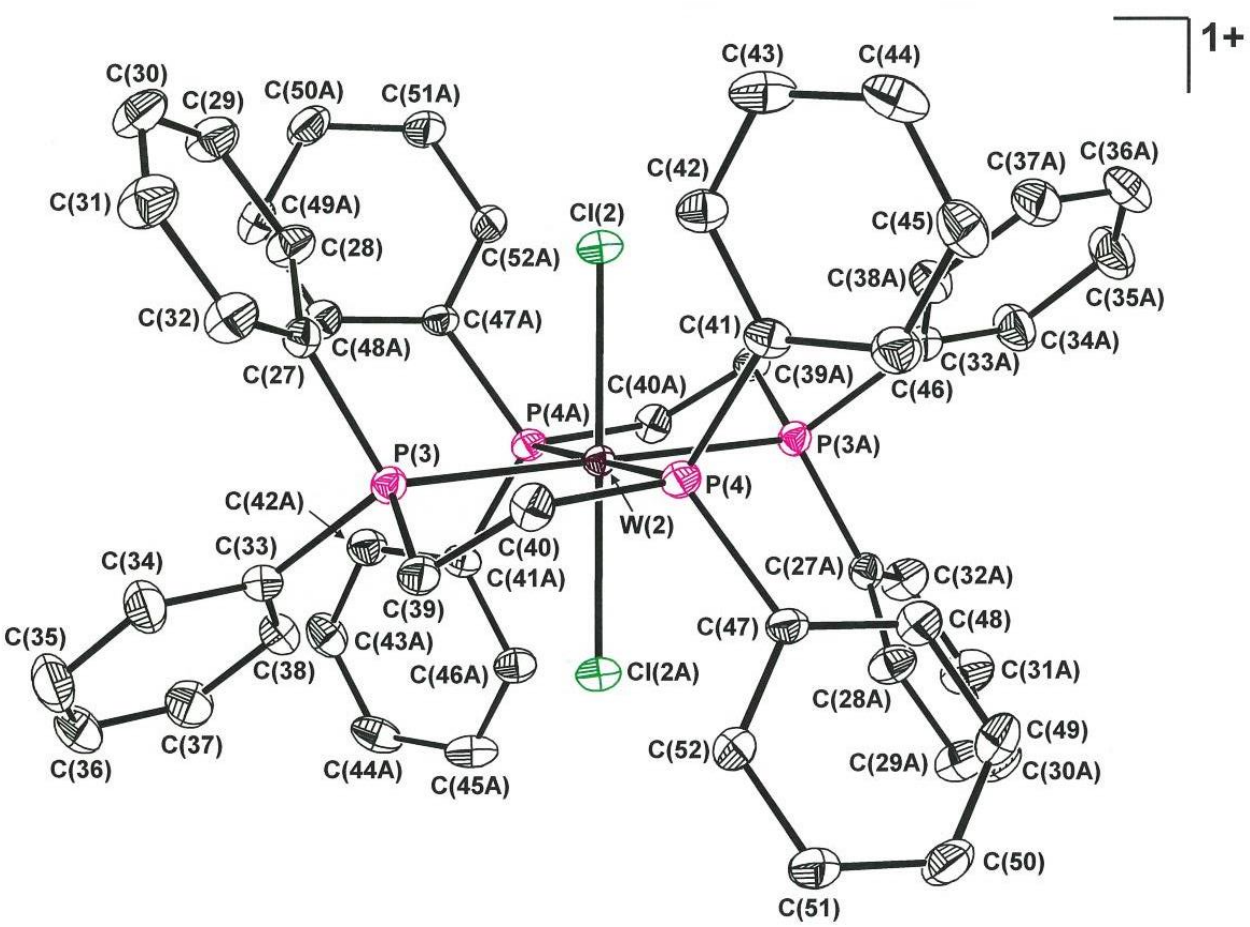

Figure S54. Thermal ellipsoid plot of cation 2 of $[W^{III}Cl_2(dppe)_2]^{1+}$ with complete atom labeling. The tungsten atom resides on an inversion center, which requires that only half of the cation be crystallographically unique. The ellipsoids are shown at the 50% probability level. Hydrogen atoms are omitted for clarity.

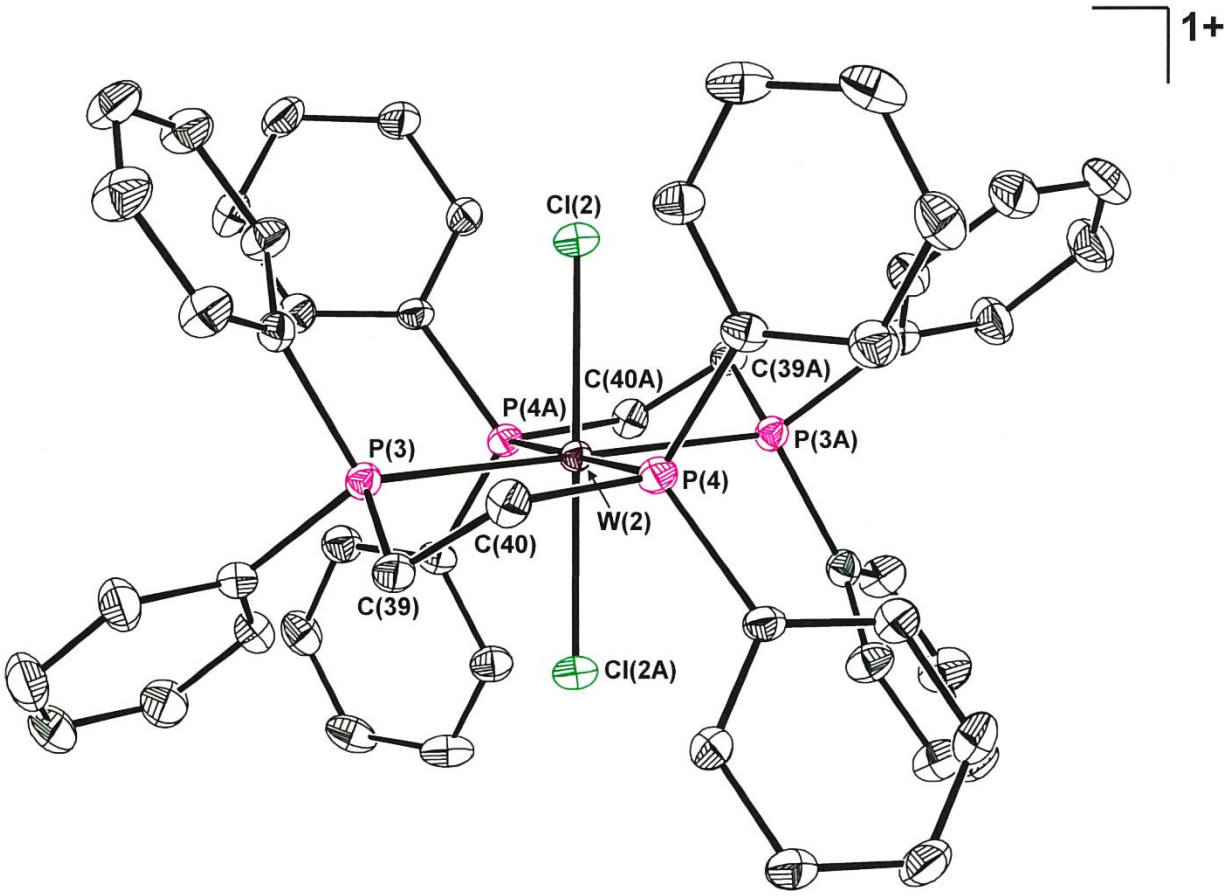

Figure S55. Thermal ellipsoid plot of cation 2 of $[W^{III}Cl_2(dppe)_2]^{1+}$ with partial atom labeling. The tungsten atom resides on an inversion center, which requires that only half of the cation be crystallographically unique. The ellipsoids are shown at the 50% probability level. Hydrogen atoms are omitted for clarity.

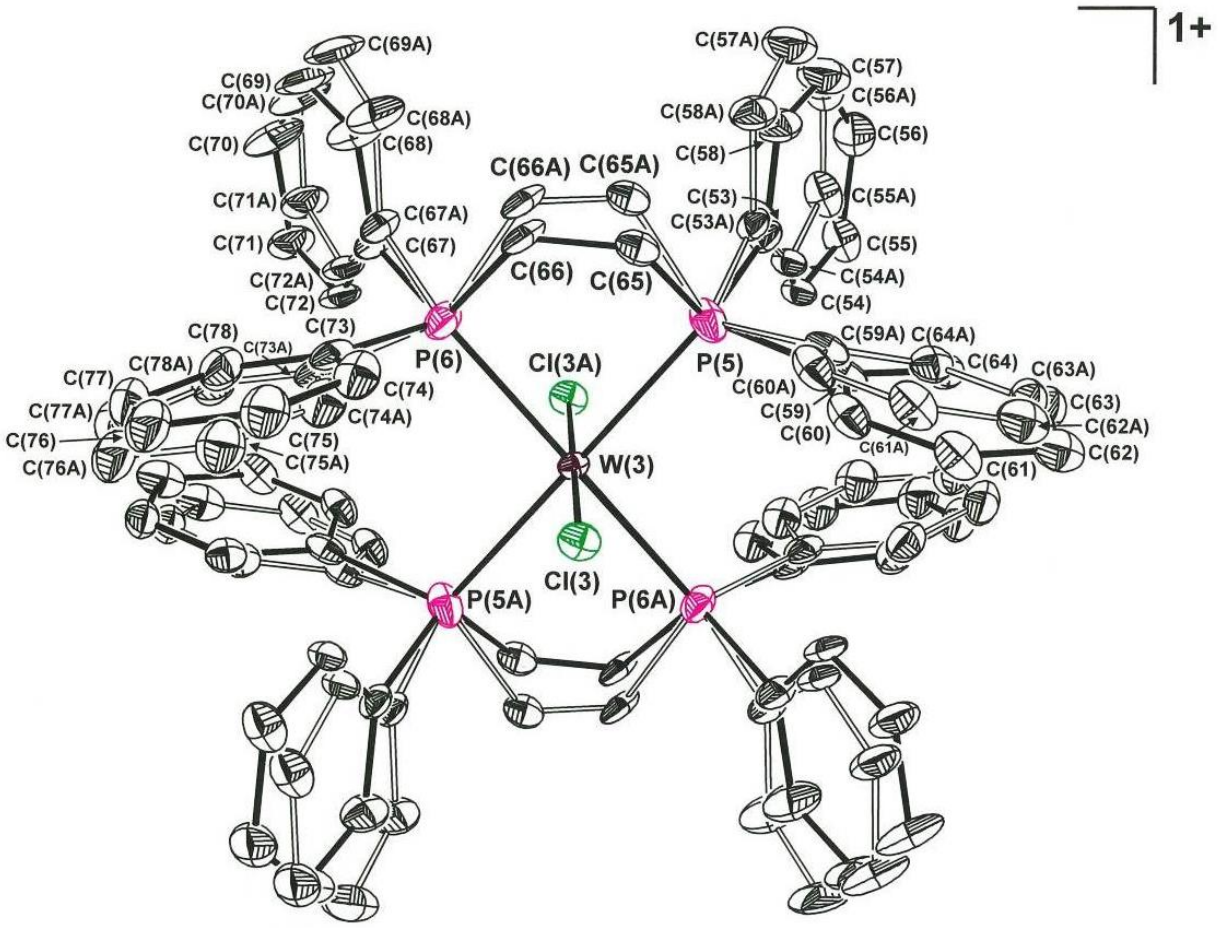

Figure S56. Thermal ellipsoid plot of cation 3 of $[W^{III}Cl_2(dppe)_2]^{1+}$ with complete atom labeling. The tungsten atom resides on an inversion center, which requires that only half of the cation be crystallographically unique. The ellipsoids are shown at the 50% probability level. Hydrogen atoms are omitted for clarity.

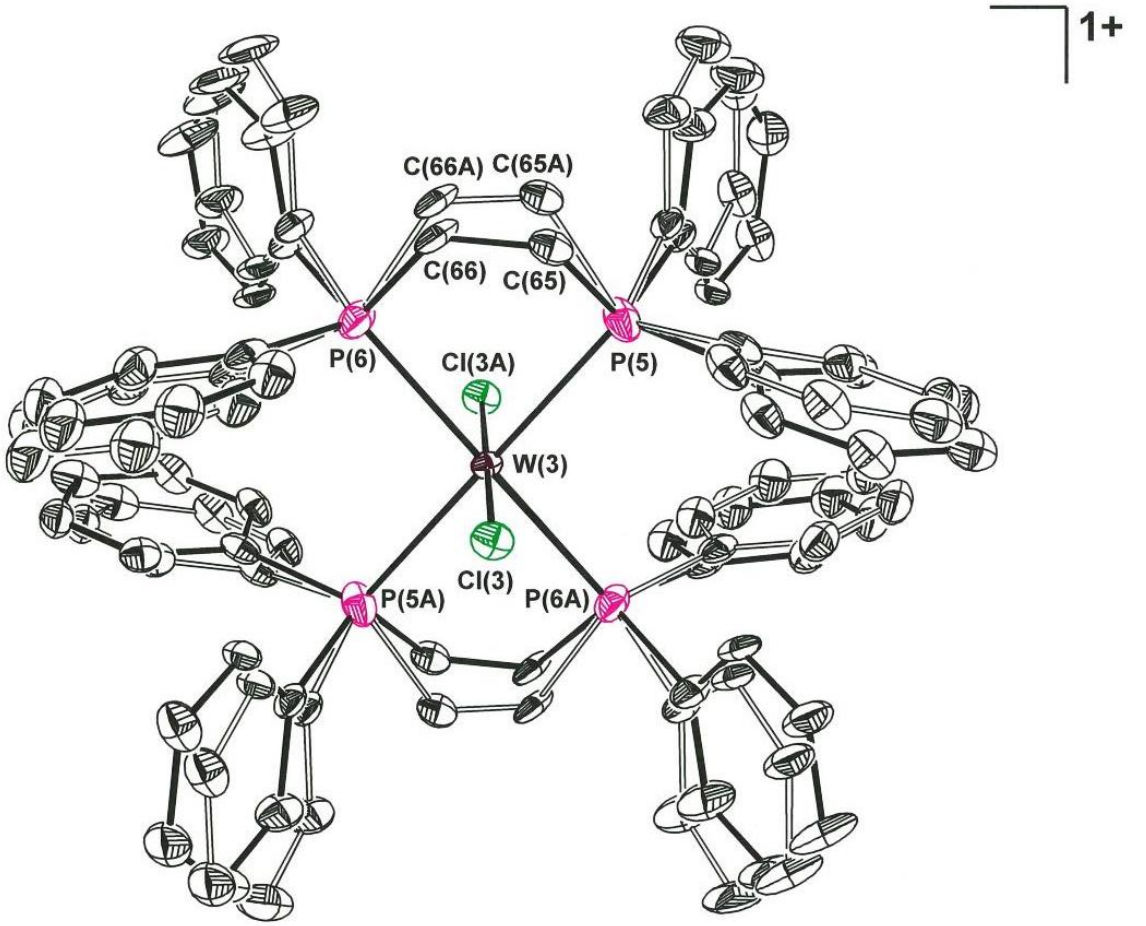

Figure S57. Thermal ellipsoid plot of cation 3 of $[W^{III}Cl_2(dppe)_2]^{1+}$ with partial atom labeling. The tungsten atom resides on an inversion center, which requires that only half of the cation be crystallographically unique. The ellipsoids are shown at the 50% probability level. Hydrogen atoms are omitted for clarity.

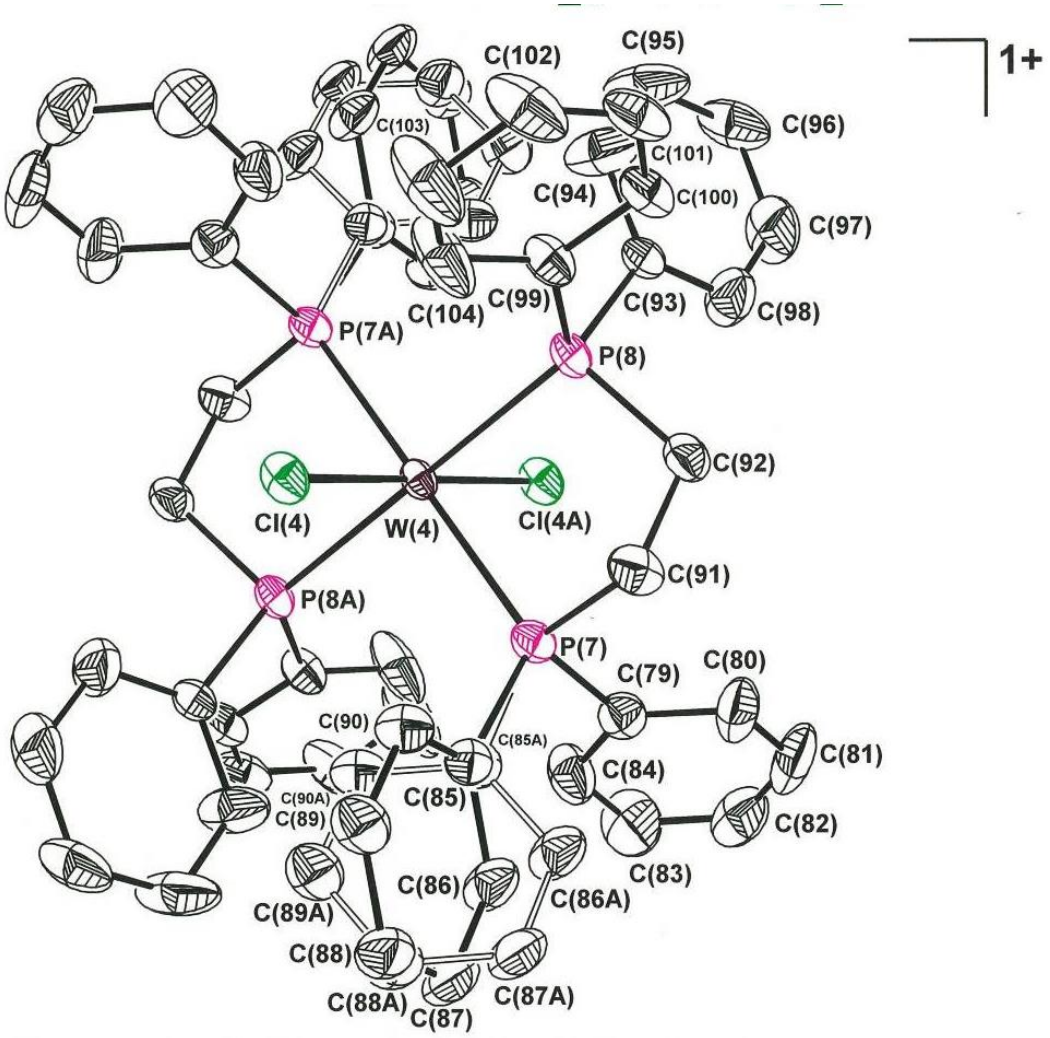

Figure S58. Thermal ellipsoid plot of cation 4 of $[W^{III}Cl_2(dppe)_2]^{1+}$ with complete atom labeling. The tungsten atom resides on an inversion center, which requires that only half of the cation be crystallographically unique. The ellipsoids are shown at the 50% probability level. Hydrogen atoms are omitted for clarity.

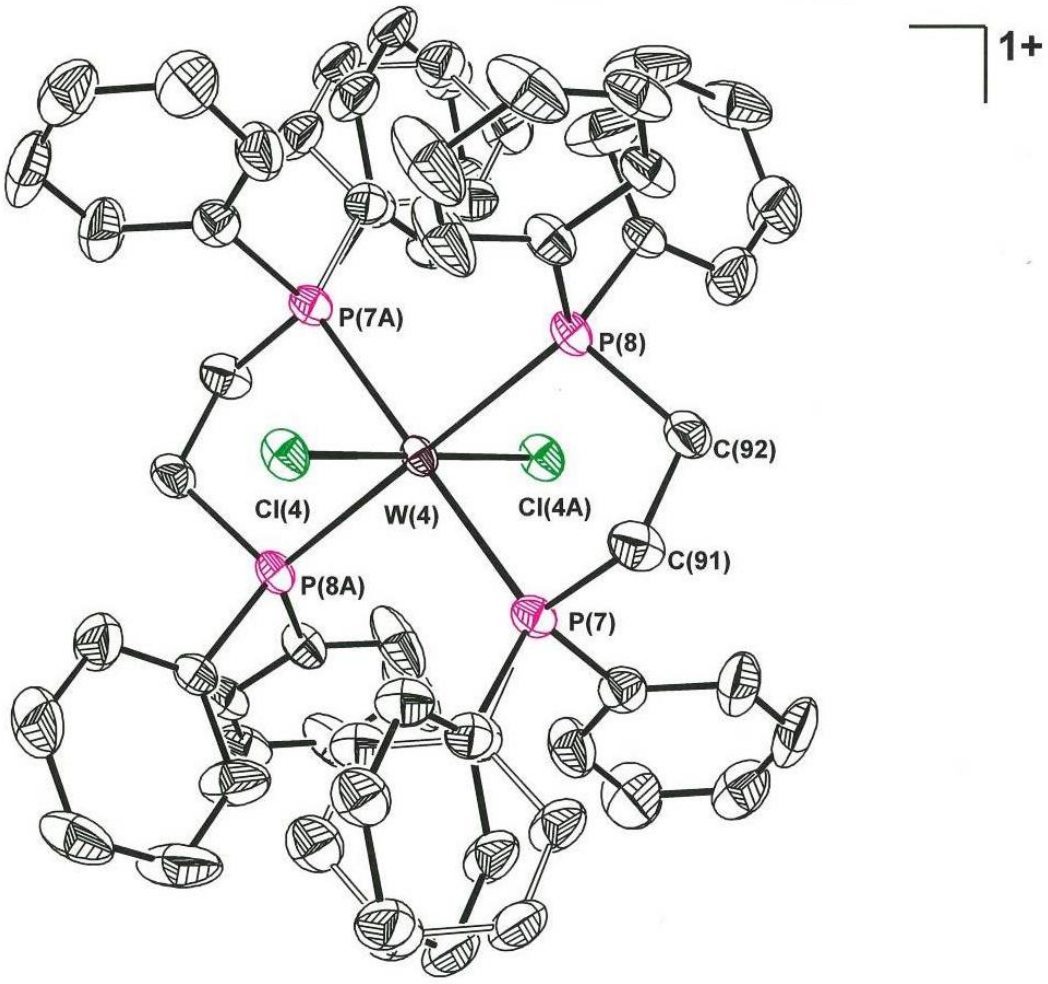

Figure S59. Thermal ellipsoid plot of cation 4 of $[W^{III}Cl_2(dppe)_2]^{1+}$ with partial atom labeling. The tungsten atom resides on an inversion center, which requires that only half of the cation be crystallographically unique. The ellipsoids are shown at the 50% probability level. Hydrogen atoms are omitted for clarity.

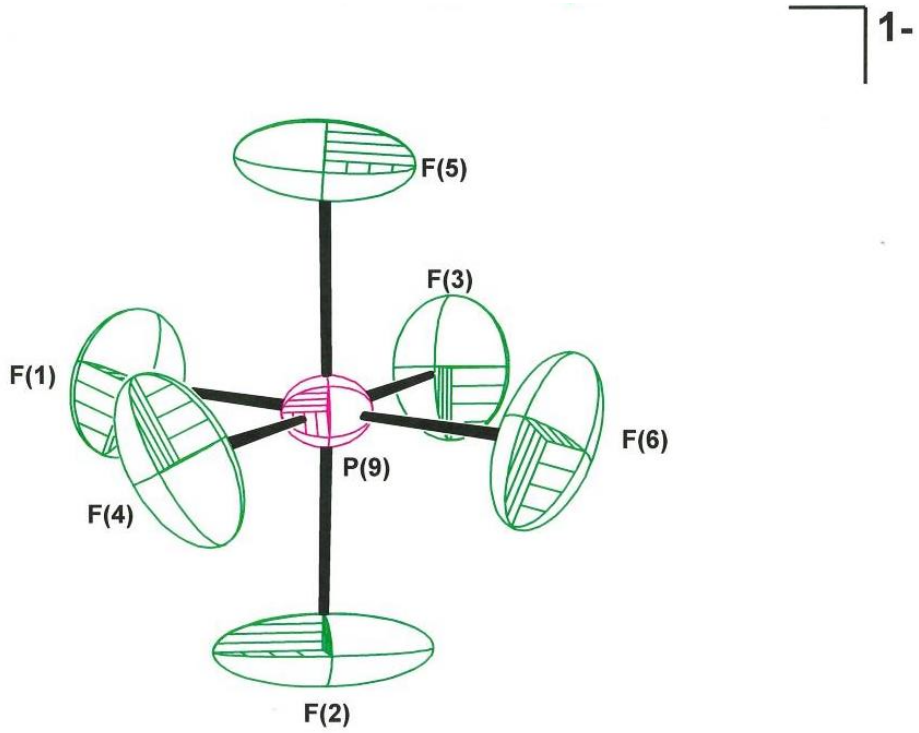

Figure S60. Thermal ellipsoid plot at the 50% probability level of anion 1 of $[PF_6]^{1-}$.

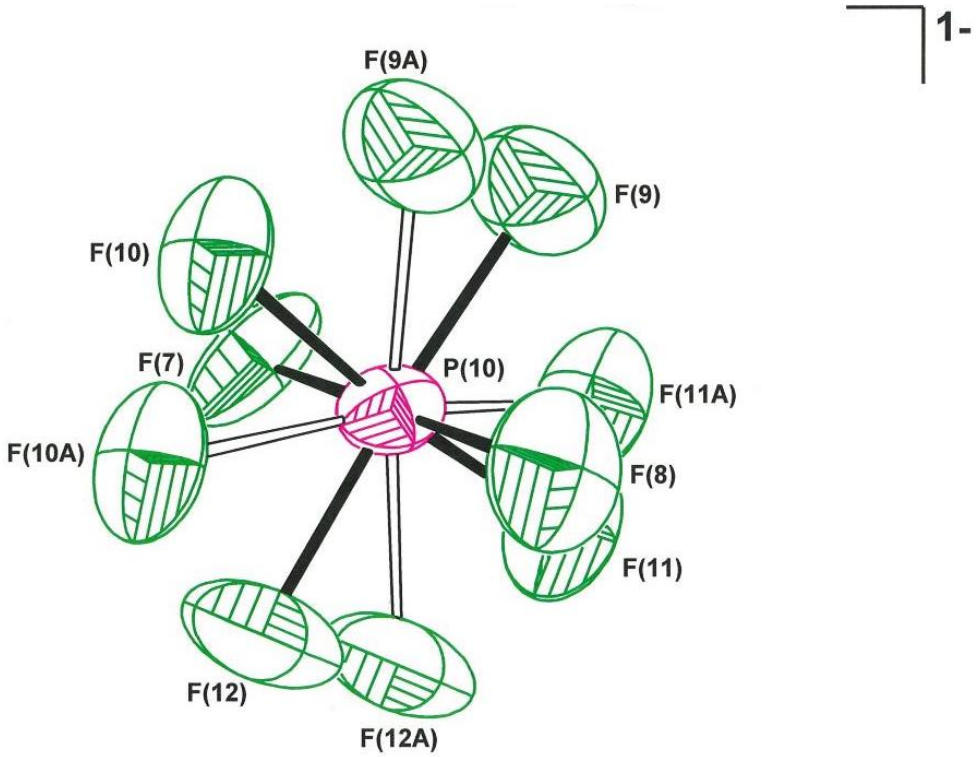

Figure S61. Thermal ellipsoid plot at the 50% probability level of anion 2 of $[PF_6]^{1-}$.

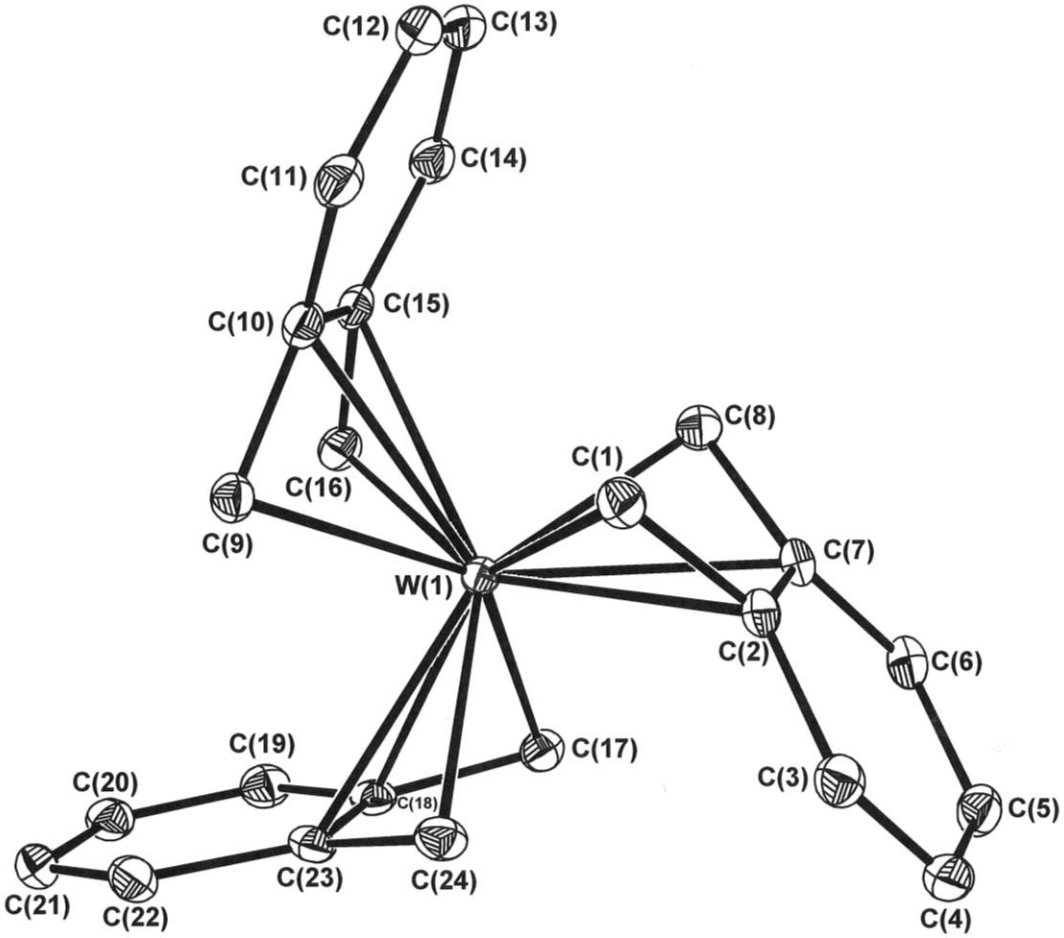

Figure S62. Thermal ellipsoid plot of [W(*o*-$(CH_2)_2C_6H_4)_3$] drawn at the 50% probability level. All hydrogen atoms are omitted for clarity.